

1 Structures of a deAMPylation complex rationalise the switch
2 between antagonistic catalytic activities of FICD (14/96/109)

3

4 Luke A. Perera^{1*}, Steffen Preissler¹, Nathan R Zaccai¹, Sylvain Prévost², Juliette M
5 Devos², Michael Haertlein², David Ron^{1*}.

6

7 1 Cambridge Institute for Medical Research, University of Cambridge, Cambridge
8 CB2 0XY, United Kingdom.

9 2 Institut Laue-Langevin, Grenoble Cedex 9, 38042, France.

10 * Address correspondence to: David Ron: dr360@medsch1.cam.ac.uk, Phone +44
11 (0)1223 768 940; or Luke A. Perera: lp397@cam.ac.uk

12

13 **Abstract**

14 The endoplasmic reticulum (ER) Hsp70 chaperone BiP is regulated by AMPylation, a
15 reversible inactivating post-translational modification. Both BiP AMPylation and
16 deAMPylation are catalysed by a single ER-localised enzyme, FICD. Here we present
17 long-sought crystallographic and solution structures of a deAMPylation Michaelis
18 complex formed between mammalian AMPylated BiP and FICD. The latter, via its
19 tetratricopeptide repeat domain, binds a surface that is specific to ATP-state Hsp70
20 chaperones, explaining the exquisite selectivity of FICD for BiP's ATP-bound
21 conformation both when AMPylating and deAMPylyating Thr518. The eukaryotic
22 deAMPylation mechanism thus revealed, rationalises the role of the conserved Fic
23 domain Glu234 as a gatekeeper residue that both inhibits AMPylation and facilitates
24 hydrolytic deAMPylation catalysed by dimeric FICD. These findings point to a
25 monomerisation-induced increase in Glu234 flexibility as the basis of an oligomeric
26 state-dependent switch between FICD's antagonistic activities, despite a similar mode
27 of engagement of its two substrates — unmodified and AMPylated BiP.

28

29 (149/150 words)

30

31 Key words: BiP, FICD, AMPylation, deAMPylation, Endoplasmic reticulum, UPR,
32 chaperone, Hsp70, PTM, adenylylation

33

34 **Introduction**

35 The endoplasmic reticulum (ER) Hsp70, BiP, dominates the chaperoning capacity of
36 the organelle¹. BiP's abundance and activity are matched to the unfolded protein load
37 of the ER at the transcriptional level, by the canonical UPR², but also post-
38 translationally³. BiP AMPylation, the covalent attachment of an ATP-derived AMP
39 moiety to the Thr518 hydroxyl group, is perhaps the best-defined BiP post-translational
40 modification. AMPylation inactivates BiP by biasing it towards a domain-docked,
41 linker-bound ATP-like Hsp70 state and away from the domain-undocked, linker-
42 extended ADP-like state⁴⁻⁶. As such, AMPylated BiP (BiP-AMP) exhibits high rates of
43 substrate dissociation and is refractory to ATPase stimulation by J-domain proteins⁴⁻⁶.
44 BiP AMPylation inversely correlates with the ER protein folding load, increasing upon
45 inhibition of protein synthesis⁷ and with resolution of ER stress⁴. Conversely, as ER
46 stress mounts, inactivated BiP-AMP is recruited into the chaperone cycle by
47 deAMPylation^{4,7,8}.

48 A single bifunctional enzyme, FICD, is responsible for both AMPylation^{4,9,10} and
49 deAMPylation¹¹⁻¹³ of BiP. FICD is the metazoan exemplar of a family of bacterial Fic
50 domain proteins¹⁴ whose canonical AMPylation activity¹⁵⁻¹⁷ is often autoinhibited by a
51 glutamate-containing alpha helix (α_{inh})^{18,19}. In FICD, the AMPylation-inhibiting
52 Glu234 is also essential for deAMPylation¹¹. Moreover, monomerisation is able to
53 reciprocally regulate FICD's AMPylation/deAMPylation activity, converting the
54 dimeric deAMPyrase into a monomeric enzyme with primary BiP AMPylating
55 functionality²⁰. The recent discovery that the *Enterococcus faecalis* Fic protein (EfFic)
56 possesses deAMPylation activity which is dependent on a glutamate homologous to
57 FICD's Glu234¹³, suggests conservation of the catalytic mechanism amongst Fic
58 enzymes. However, the role of Glu234 in the oligomeric state-dependent regulation of
59 FICD's mutually antagonistic activities remains incompletely understood.

60 Fic domain proteins are unrelated to the two known bacterial deAMPylating enzymes,
61 SidD and the bifunctional GS-ATase. Both catalyse binuclear Mg²⁺-facilitated
62 deAMPylation reactions of a hydrolytic²¹ and phosphorolytic²² nature, utilising a metal-
63 dependent protein phosphatase²¹ and nucleotidyl transferase^{23,24} protein-folds,
64 respectively. Fic proteins have a single divalent cation binding site and are

65 evolutionarily and structurally divergent from these deAMPylases and, therefore, likely
66 catalyse a distinct deAMPylation mechanism.

67 In addition to the aforementioned enzyme-based regulatory mechanism(s), there is
68 evidence that AMPylation is also regulated by substrate availability. Cells with a
69 constitutively monomeric FICD retain a measure of regulated BiP AMPylation²⁰. FICD
70 specifically binds and AMPylates the domain-docked ATP-state of BiP^{4,20}. Client
71 binding partitions Hsp70s away from their ATP-state, suggesting a simple mechanism
72 for coupling BiP AMPylation to low protein folding loads. Furthermore, the finding
73 that FICD selectively AMPylates and deAMPylates ATP-state biased BiP suggests that
74 FICD may recognise ATP-state specific features of its substrate in a conserved binding
75 mode, that is independent of FICD's oligomeric-state or BiP modification status.

76 Here we present a structure-based approach to determine the nature of the FICD-BiP
77 enzyme-substrate interaction, thereby elucidating the mechanism of eukaryotic
78 deAMPylation and the basis for its regulation by an oligomerisation-based switch in
79 FICD's functionality.

80 **Results**

81 **FICD engages AMPylated BiP and primes a Glu234-coordinated water molecule**
82 **for nucleophilic attack**

83 Mutation of the Fic motif catalytic histidine, which acts as an essential general base in
84 the AMPylation reaction^{15,16,25}, eradicates FICD's deAMPylation activity¹¹. Upon
85 mutation of this histidine (His363Ala) FICD and BiP-AMP formed a long-lived,
86 trapped deAMPylation complex²⁰. This feature was exploited to copurify FICD and
87 AMPylated BiP by size exclusion chromatography (SEC). A complex of otherwise
88 wildtype dimeric FICD^{H363A} and AMPylated BiP readily crystallised, but despite
89 extensive efforts, these crystals did not yield useful diffraction data. However,
90 introduction of a monomerising Leu258Asp mutation and truncation of BiP's flexible
91 α -helical lid yielded a heterodimeric FICD^{L258D-H363A}•BiP^{T229A-V461F}-AMP complex
92 (Fig. 1a; see methods) that crystallised and yielded two very similar sub-2 Å datasets
93 (Table 1).

94 The crystal structures displayed (identical) extensive bipartite protein-protein interfaces
95 totalling 1366 Å² (Fig. 1b and Supplementary Fig. 1a; state 1 crystal structure is
96 shown). The deAMPylation substrate, AMPylated BiP, is in a domain-docked ATP-
97 like state (despite having hydrolysed its bound MgATP), as reflected by the similarity
98 with the isolated ATP-state BiP-AMP structure⁵ (Fig. 1b(i); 1.02 Å RMSD across all
99 521 C α pairs). The FICD tetratricopeptide repeat domain motif 1 (TPR1) contacted a
100 tripartite BiP surface (695 Å²), comprised of its nucleotide binding domain (NBD),
101 interdomain linker and substrate binding domain- β (SBD β) (Fig. 1b(ii), left panel). The
102 second interface, by which FICD's catalytic Fic domain engaged BiP's SBD β (671 Å²),
103 contained an intermolecular β -sheet between BiP's Thr518 bearing loop ($\ell_{7,8}$) and the
104 Fic domain flap (implicated in a bacterial Fic protein AMPylation-substrate
105 binding^{16,19}). The AMP, covalently attached to BiP's Thr518, was inserted into the Fic
106 domain active site, with the adenine occupying the same position as in
107 FICD:nucleotide complexes^{20,25} (Fig. 1b(ii) right panel and Supplementary Fig. 1b).
108 Contacts between the AMP moiety and the FICD active site contributed an additional
109 306 Å² interaction surface to the deAMPylation complex.

110 Monomeric FICD retains deAMPylation activity^{12,20}, although reduced relative to that
111 of the dimeric enzyme²⁰. Superposition of two monomeric FICD-containing

112 deAMPylation complexes (state 1) with a dimeric FICD structure (PDB 4U0U; 2.58 Å
113 RMSD over 334 C α pairs across each FICD protomer), demonstrates that the
114 heterodimeric deAMPylation crystal structure is compatible with a deAMPylation
115 complex of dimeric FICD engaging two full-length BiP-AMP molecules (**Fig. 1c**).
116 Furthermore, the schematised unstructured linker between the N-terminus of FICDs'
117 TPR domains and the ER membrane (**Fig. 1c**) illustrates that the modelled
118 heterotetrameric structure is compatible with FICD's presumed orientation within the
119 ER^{25,26}. Moreover, the alignment with dimeric FICD reveals intra-TPR domain
120 movement away from FICD's catalytic core (especially in the TPR1 motif region),
121 which likely results from the interaction with the tripartite BiP surface.

122 The deAMPylation complex crystal structure contains well-resolved electron density
123 for BiP's AMPylated Thr518 residue within FICD's active site (**Fig. 1d**). The
124 phosphate of Thr518-AMP is coordinated by a Mg²⁺ held in position by FICD's
125 Asp367. A similarly-positioned Mg²⁺ coordinates the α and β phosphates of ATP in
126 the AMPylation-competent enzyme²⁰. Glu234 (located atop the α_{inh}) tightly engages a
127 water molecule within FICD's oxyanion hole (**Fig. 1d** and **Supplementary Fig. 1b**).
128 The latter Fic domain feature contributes towards the stabilisation of ATP's α and
129 β phosphates in the AMPylating enzyme.

130 The aforementioned Glu234-coordinated water molecule sits almost directly in-line
131 with the P α -O γ (Thr518) phosphodiester bond (**Fig. 1e** and **Supplementary Fig. 1b**)
132 and likely participates in catalysis. When also modelled with a catalytic histidine (from
133 PDB 6I7K; 0.45 Å RMSD over 214 C α pairs aligned over the Fic domain residues 213–
134 426) the structure is highly suggestive of an acid-base hydrolytic mechanism of
135 eukaryotic deAMPylation: Glu234 aligns and activates a water molecule for an S_N2-type
136 nucleophilic attack into the α -phosphate with His363 positioned to facilitate a
137 concerted protonation of the Thr518 alkoxide leaving group (generating unmodified
138 BiP and AMP as products¹¹).

139 **The deAMPylation complex crystal structure is representative of the solution**
140 **structure of dimeric FICD engaged with AMPylated BiP**

141 To assess the validity of the structural insights gained from the heterodimeric
142 deAMPylation complex crystal (obtained with monomeric FICD^{L258D-H336A} and a lid-
143 truncated BiP-AMP), a solution-based structural method was employed using intact

144 proteins. Low-resolution structures of biomacromolecules can be resolved by small
145 angle X-ray and neutron scattering (SAXS/SANS). SAXS is sensitive to electron
146 density, while SANS is sensitive to atomic nuclei. For mixed complexes with two
147 components, contrast variation SANS is able to distinguish between proteins that are
148 differentially isotopically labelled. To enable this analysis, complexes of partially
149 deuterated and non-deuterated dimeric FICD^{H363A} and full-length BiP-AMP were
150 copurified by SEC into buffers with varying D₂O content. Contrast variation solution
151 scattering data were subsequently collected (**Fig. 2a**).

152 Analysis of the low-*q* Guinier region (**Fig. 2b** and **Supplementary Fig. 2a**) provided
153 information pertaining to the forward scattering, *I*(0), and radius of gyration, *R*_g, in each
154 solution. The former, along with calculation of each complex's contrast match point
155 (CMP; **Fig. 2c**), permitted the estimation of the complex molecular weight
156 (**Supplementary Table 1**) — which was in good agreement with a FICD•BiP-AMP
157 2:2 complex. The Stuhrmann plot (derived from the square of the *R*_g data against the
158 reciprocal of the contrast)²⁷ provided information on the internal arrangement of the
159 heterotetramer (assigning FICD to the inside of the complex) and size (*R*_g) of the overall
160 complex and its constituent components; all of which are consistent with those
161 calculated from the modelled heterotetramer structure (**Fig. 2d** and **Supplementary**
162 **Table 1**).

163 The Stuhrmann plot's shape provides additional information. The relatively linear
164 Stuhrmann plot derived from the deAMPylation complex containing partially
165 deuterated FICD, suggests that this complex has a scattering length density (SLD)
166 centre which is very close to the complexes centre of mass (COM). The converse is true
167 for the partially deuterated BiP complex's Stuhrmann fit that reveals no overlap
168 between the latter's SLD centre and COM. As partial-deuteration of a component
169 increases its relative contribution to the SLD, these findings are consistent with a
170 heterotetramer in which the centre of mass lies in the plane of the FICD dimer and
171 above the plane of the majority of the BiP mass. This arrangement fits well the
172 structural model presented in **Fig. 1c**.

173 Moreover, across the scattering range and at all D₂O concentrations, the theoretical
174 scattering profile of the heterotetramer (modelled in **Fig. 1c**) correlated well with the
175 observed experimental scattering, with an overall average χ^2 of 3.4 ± 4 (mean \pm SD) or
176 2.4 ± 2 following anomalous dataset removal (**Fig. 2a** and **Supplementary Fig. 2b**).

177 This was true even at D₂O concentrations close to the CMP for each deAMPylation
178 complex, where the scattering profile is very sensitive to both the shape and
179 stoichiometry of the particles in solution. Furthermore, the best flex-fit structure
180 (generated for each scattering dataset by allowing the input structure to undergo normal
181 mode flexing of its domains) did not significantly improve model fitting. The SANS
182 data thus indicate that the vast majority of particles in solution are engaged in a
183 heterotetramer with neutron scattering properties predicted by a model based on the
184 heterodimer crystal structure.

185 By analysing the data over the entire scattering *q*-range, through flex-fitting, it is also
186 possible to capture some of the dynamics of the solution structure. Although no
187 individual flex-fit structure produced a significantly reduced average χ^2 across all
188 datasets, a number of flex-fit output structures did have significantly different and
189 reduced χ^2 variance (**Supplementary Fig. 2c**, underlined). The majority of flex-fit
190 structures possessed R_g parameters which were in good agreement with the Stuhrmann
191 derived R_g values (**Supplementary Fig. 2d**) and the principal variation in the flex-fit
192 structures was evident in BiP(NBD) and FICD(TPR) domain reorientation and in the
193 BiP lid region (**Supplementary Fig. 2e–f**). Only around half of the flex-fit output
194 structures maintained the C2 rotational symmetry present in the input heterotetramer
195 structure (**Supplementary Fig. 2c–d**, bold), which stems from the C2 symmetry of the
196 FICD dimer. As symmetry is expected for an average solution structure of a
197 (symmetrical) dimeric FICD fully occupied at two independent BiP binding sites, each
198 flex-fitting strategy yielded only best-fit structure which was both symmetrical and had
199 a significantly reduced χ^2 SD (**Fig. 2e**, **Supplementary Fig. 2g**, **2c–d** bold and
200 underlined and **Supplementary Movie 1**). The best-fit structure derived from leaving
201 the high affinity FICD dimer interface unconstrained (mean χ^2 goodness-of-fit across
202 the reduced data set 1.7 ± 0.4) is closer in conformation to the input structure than that
203 obtained with a restrained dimer-interface (mean $\chi^2 2.4 \pm 0.8$), with an RMSD of 5.4
204 and 7.1 Å (across 1,892 C α pairs), respectively. Both output structures demonstrate
205 good R_g agreement with the Stuhrmann analysis. Importantly, the complexes' FICD R_g s
206 are increased, and in better agreement with the experimentally derived values, relative
207 to the input structure (**Supplementary Fig. 2d** and **Supplementary Table 1**).
208 Therefore, the observed model deviation is indicative of additional deAMPylation
209 complex flexibility in solution, in particular in the composite FICD(TPR)-BiP(NBD)

210 interface and in the disposition of the BiP lid. This flexibility is inaccessible to
211 crystallographic analysis of BiP (complexes) but is consistent with previous
212 observations of Hsp70 conformational dynamics in the Hsp70 ATP-state^{6,28}.

213 **Engagement of the FICD TPR domain with BiP-AMP is essential for complex**
214 **assembly and deAMPylation**

215 To test the importance of contacts between FICD's TPR domain and BiP in complex
216 formation, catalytically inactive (His363Ala) but structurally intact FICD variants
217 (**Supplementary Fig. 3a–c**) were analysed for their ability to interact with immobilised
218 BiP by BioLayer Interferometry (BLI). As FICD selectively binds to the ATP-state of
219 BiP²⁰, BiP was pre-incubated with MgATP (**Supplementary Fig. 3d**). Consistent with
220 previous findings²⁰, BiP bound more tightly to monomeric FICD^{L258D-H363A} than to
221 dimeric FICD. The converse was true for AMPylated BiP. Complex dissociation was
222 further accelerated by the addition of ATP to the dissociation buffer (**Fig. 3a**); via an
223 allosteric effect on FICD, when engaging unmodified BiP:ATP, or by competition for
224 FICD's active site when engaging BiP-AMP²⁰. However, upon removal of the TPR1
225 motif, dimeric FICD lost all appreciable binding to either BiP ligand. As predicted by
226 the mode of TPR binding in the crystal structures, the isolated TPR domain measurably
227 interacted with BiP ligands irrespective of their modification status.

228 The introduction of point-mutations into residues at the FICD(TPR1)-BiP interface
229 (**Fig. 1b** and **Supplementary Fig. 1a**) significantly affected the kinetics of FICD
230 association and dissociation of both monomeric and dimeric FICD variants (**Fig. 3b**).
231 This agrees with the idea (supported by the solution structure) that monomeric and
232 dimeric FICD similarly engage AMPylated BiP. Moreover, in keeping with the
233 crystallographically observed multivalent nature of the deAMPylation complex, the
234 kinetics of FICD^{L258D-H363A}•BiP-AMP interaction appears biphasic and becomes
235 increasingly monophasic upon disruption of FICD(TPR1)-BiP contacts (**Fig. 3b(i)**).

236 To address the role of interdomain contacts between FICD's TPR and catalytic Fic
237 domain in deAMPylation complex stability, one of two contacting residues within
238 FICD's TPR2 motif (Asp160) was mutated (**Fig. 1b(ii)**). However, FICD's TPR
239 domain has also been observed to fully disengage from the capping/linker helix,
240 exhibiting a 'TPR-out' conformation (PDB 6I7K and 6I7L). To analyse the effect of
241 perturbed interdomain contacts, whilst maintaining the BiP binding-competent 'TPR-

242 in' conformation, Asp160 and Thr183 (FICD capping helix; **Fig. 1b(ii)**) were both
243 mutated to cysteines and oxidised to stoichiometrically form an intramolecular
244 disulphide bond (TPRox, **Supplementary Fig. 3c**). TPR oxidation within monomeric
245 FICD^{L258D-H363A} resulted in more biphasic kinetics and a significant decrease in
246 dissociation rate from BiP (**Fig. 3b(i)**), suggesting that the covalent fixation of the
247 'TPR-in' conformation outweighs the destabilising effects of perturbing the
248 intramolecular Fic-TPR domain contact. Notably, the effect on dimeric FICD was less
249 pronounced (**Fig. 3b(ii)**). These measurements are consistent with the fact that the
250 'TPR-out' conformation has only been observed in monomeric FICD structures²⁰ and
251 suggest that dimeric FICD has an intrinsically less flexible TPR domain. Nevertheless,
252 TPR oxidation does alter dimeric FICD binding kinetics. The increased FICD
253 dissociation rate, which is further exaggerated by the addition of ATP in the second
254 dissociation phase, implicates Fic-TPR domain communication in the regulation of
255 complex association-dissociation kinetics.

256 Consistent with the essential role played by the TPR domain in deAMPylation complex
257 assembly, mutation or removal of the TPR1 motif reduced the catalytic efficiency
258 (k_{cat}/K_M) of in vitro deAMPylation (**Fig. 3c**, top, and **Supplementary Fig. 3e–g**). As
259 expected from previous analysis of FICD-mediated deAMPylation under substrate-
260 limited conditions²⁰, monomerisation of FICD was observed to diminish the rate of
261 deAMPylation under a steady-state kinetic regime (**Fig. 3c**, bottom). Interestingly,
262 having not significantly decreased the observed affinity for AMPylated BiP, TPR
263 domain oxidation appreciably compromised the deAMPylation activity of both
264 monomeric and dimeric FICD (**Fig. 3c**, bottom). This effect on catalytic efficiency
265 presumably reflects a contribution of TPR domain flexibility or intra-FICD interdomain
266 communication towards deAMPylation turnover number (k_{cat}).

267 **FICD's TPR domain is responsible for the recognition of unmodified ATP-state 268 BiP**

269 The importance of contacts between FICD's TPR domain and BiP to deAMPylation,
270 demonstrated above, explains previous observations that the isolated AMPylated BiP
271 SBD is refractory to FICD-mediated deAMPylation¹¹. It is noteworthy that FICD also
272 specifically binds²⁰ and AMPylates ATP-state BiP with a preference for more domain-
273 docked BiP mutants and fails to AMPylate the isolated BiP SBD⁴. Furthermore, the

274 observation that FICD's interaction with unmodified BiP:ATP was abrogated by TPR1
275 deletion (**Fig. 3a**) hints at the possibility that FICD recognises the ATP-state of
276 unmodified BiP (for AMPylation) in a similar fashion to ATP-state biased BiP-AMP
277 (for deAMPylation).

278 Structures of unmodified BiP indicate that a domain-undocked ADP-state BiP loses the
279 tripartite NBD-linker-SBD β surface that is recognised by FICD's TPR1 motif in the
280 context of deAMPylation (**Supplementary Fig. 4a** and **Supplementary Movie 2**).
281 Furthermore, even if FICD were able to bind the NBD or the $\ell_{7,8}$ SBD β region (which
282 also becomes less accessible in BiP's ADP-state) of a nucleotide-free (apo) or ADP-
283 bound BiP, the Hsp70's heavy bias towards the domain-undocked conformation^{6,29}
284 would render engagement of the other FICD-BiP interaction surface unlikely
285 (**Supplementary Fig. 4a** and **Supplementary Movie 2**).

286 To test the potential role of conserved TPR-BiP contacts in formation of an AMPylation
287 complex we returned to the BLI setup of **Fig. 3b**, but with ATP-bound unmodified BiP
288 immobilised as a ligand. In this context the effect of TPR1 motif mutations on FICD
289 binding were magnified relative to their effect on the deAMPylation complex (**Fig. 4a**).
290 This is consistent with the absence of a covalently linked AMP moiety, engaging FICD's
291 active site, increasing the relative contribution of TPR-BiP contacts to the overall
292 complex interaction. Loss of TPR-BiP contacts by surface mutations in TPR1 also
293 impaired BiP AMPylation by monomeric FICD in vitro (**Fig. 4b** and **Supplementary**
294 **Fig. 4b**), paralleling the effect of these mutations on deAMPylation complex assembly
295 and in vitro deAMPylation activity (**Fig. 3**). Of note, impairment of interdomain (TPR-
296 Fic) communication by TPR oxidation, although stabilising the pre-AMPylation
297 complex of monomeric FICD and BiP:ATP (**Fig. 4a**), decreases the in vitro
298 AMPylation rate.

299 To examine the effect of the TPR surface mutations on BiP AMPylation in cells, we
300 compared the ability of otherwise wildtype, hyperactive, monomeric FICD lacking the
301 gatekeeper glutamate (FICD^{E234G-L258D}) and TPR mutant versions thereof to promote a
302 pool of AMPylated BiP in cells. Levels of AMPylated BiP, detected by its mobility on
303 native-PAGE, were significantly lower in cells targeted with the FICD^{K124E-E234G-L258D}
304 and FICD^{K124E-H131A-E234G-L258D} TPR1 mutations (**Fig. 4c**). The higher levels of
305 expression of the TPR1 mutant FICDs (compared to FICD^{E234G-L258D}) is consistent with

306 previous observations of FICD expression levels inversely correlating with the
307 variant's AMPylation activity (within transiently transfected *FICD*^{-/-} cells)²⁰.

308 BiP inactivation, by deregulated AMPylation, can cause considerable ER stress²⁰. This
309 feature was exploited to quantify the functional effect of the TPR1 mutations in an
310 orthogonal assay, based on the ER stress-responsive reporter XBP1::Turquoise,
311 utilising flow cytometry (**Fig. 4d** and **Supplementary Fig. 4c**). In cells expressing the
312 various TPR1 mutant FICD derivatives, reporter activity (analysed by its bimodal
313 distribution) correlated well with the levels of AMPylated BiP detected by native-
314 PAGE and with the hierarchy of the mutations' effects on BiP binding (**Fig. 3b**).
315 Together these observations lead us to conclude that TPR surface mutations in residues
316 that contact BiP in the deAMPylation complex also contribute to enzyme-substrate
317 interaction during FICD-induced AMPylation. Moreover, BiP's Th518 can be readily
318 modelled into the active site of a AMPylating monomeric FICD alongside its MgATP
319 co-substrate, by alignment with the deAMPylation complex's Fic domain
320 (**Supplementary Fig. 4d**). This provides further support for there being a similar mode
321 of FICD substrate engagement in its mutually antagonistic enzymatic activities.

322 **Increased Glu234 flexibility enfeebles monomeric FICD deAMPylation activity**

323 The deAMPylation complex presented in **Fig. 1** explains the essential role of
324 gatekeeper Glu234 in Fic domain-catalysed deAMPylation^{11,13}. However, a second
325 sub-2 Å deAMPylation complex-crystal structure, which is almost identical to that
326 previously presented (**Table 1**, **Supplementary Fig. 5a** and **Supplementary Movie 1**),
327 hints at an important detail. As in the state 1 structure (**Fig. 1**), the FICD active site
328 contains clear electron densities for BiP's Thr518-AMP, Fic domain catalytic residues
329 and a coordinated Mg²⁺ cation (**Supplementary Fig. 5a**). However, alignment with the
330 state 1 structure reveals a clear difference in the orientation of Glu234 (**Fig. 5a**,
331 **Supplementary Fig. 5c** and **Supplementary Movie 3**). In the second, state 2, structure
332 the Glu234 sidechain points further away from the position of the catalytic water
333 molecule, that was so clearly visible in state 1, and more towards Mg²⁺.

334 The variability in Glu234 conformation noted above fits previous observations that
335 FICD monomerisation increases Glu234 flexibility, disfavouring autoinhibition of
336 AMPylation activity²⁰. The reorientation of Glu234 noted in state 2 also informs the
337 deAMPylation reaction, as it results in a slight shift in the Mg²⁺ octahedral coordination

338 complex (**Fig. 5a** and **Supplementary Movie 3**). Although there is some remaining
339 electron density in the region of the catalytic water molecule noted in state 1, this
340 density merged with the electron density of a Mg^{2+} -coordinating water molecule. The
341 elongated density is incompatible with the modelling of two water molecules
342 (accommodating the Mg^{2+} -coordination geometry requirements would necessitate an
343 infeasible inter-water distance of 1.89 Å) and suggests that there may be a dynamic
344 shuttling of a water to and from the primary Mg^{2+} -coordination sphere into a position
345 more conducive to catalysis. It is clear that the Glu234 position observed in the state 2
346 crystal structure does not permit the stable positioning of a catalytic water molecule in-
347 line for nucleophilic attack.

348 A corollary of the two tenets, that Glu234 is necessary for coordinating a catalytic water
349 molecule for deAMPylation and that Glu234 flexibility increases upon
350 monomerisation, is the prediction that FICD deAMPylation activity should decrease
351 upon monomerisation. This has already been demonstrated in terms of a 46% decrease
352 in catalytic efficiency (**Fig. 3c**) — the calculated k_{cat}/K_M of FICD ($630 \pm 50 \text{ s}^{-1} \text{ M}^{-1}$,
353 mean \pm SEM) is 1.9-fold greater than that of $FICD^{L258D}$ ($340 \pm 30 \text{ s}^{-1} \text{ M}^{-1}$). Moreover,
354 dimeric FICD's k_{cat}/K_M is in good agreement with that derived from a previous
355 Michaelis-Menten analysis of a GST-tagged FICD ($600 \pm 100 \text{ s}^{-1} \text{ M}^{-1}$, best-fit \pm SE)¹¹.

356 However, an increase in Glu234 flexibility is expected to intrinsically affect
357 deAMPylation catalysis and lower the k_{cat} . In order to directly measure the turnover
358 number for monomeric and dimeric FICD both enzymes must be saturated with
359 deAMPylation substrate. It was found that the initial rates of deAMPylation were
360 indistinguishable at initial substrate concentrations of 100 and 150 μM BiP-AMP (**Fig.**
361 **5b** and **Supplementary Fig. 5d–e**), implying that FICD and $FICD^{L258D}$ are saturated
362 by BiP-AMP. Therefore, at these substrate concentrations the initial deAMPylation
363 rates represent maximal enzyme velocities, from which a k_{cat} parameter can be extracted
364 (**Fig. 5c**). As expected for the less-flexible Glu234-bearing dimeric FICD, its
365 deAMPylation k_{cat} ($\{10 \pm 1\} \times 10^{-3} \text{ s}^{-1}$, mean \pm SEM) was significantly greater (1.8-
366 fold) than that of monomeric $FICD^{L258D}$ ($\{5.7 \pm 0.4\} \times 10^{-3} \text{ s}^{-1}$).

367 Together, the comparison of deAMPylation catalytic efficiencies and turnover numbers
368 between dimeric and monomeric FICD, suggests that the major effect of
369 monomerisation on the kinetics of deAMPylation is mediated through a decrease in k_{cat} .
370 Thus, despite the apparent differences between monomeric and dimeric FICD in their

371 affinity for BiP-AMP (**Fig. 3a**), any differences in K_D must be compensated for by the
372 variation in k_{cat} values — resulting in very similar K_M values of $16 \pm 2 \mu\text{M}$ for dimeric
373 and $17 \pm 2 \mu\text{M}$ for monomeric FICD (mean \pm SEM). Note, the k_{cat} and K_M values
374 derived for dimeric FICD are in good agreement with those previously obtained from
375 Michaelis-Menten analysis of GST-FICD: $k_{cat} \{9.9 \pm 0.9\} \times 10^{-3} \text{ s}^{-1}$ and $K_M 16 \pm 3 \mu\text{M}$
376 (best-fit \pm SE)¹¹, adding credibility to the k_{cat}/K_M and K_M determinations.

377 **Discussion**

378 Here, we have leveraged insights from crystal structures of a deAMPylation complex
379 (the first such structure to our knowledge) of FICD and BiP-AMP to gain a detailed
380 understanding of eukaryotic deAMPylation and a broad understanding of the enzyme-
381 substrate interactions of FICD that underpin its mutually antagonistic activities of BiP
382 AMPylation and deAMPylation. Biochemical and cellular studies of structure-guided
383 mutations in FICD have shed light on both substrate level and enzyme-level regulation
384 of BiP's AMPylation cycle as it matches BiP activity to ER stress in a post-translational
385 strand of the UPR (**Fig. 6**).

386 The specific recognition of ATP-state BiP is mediated by an interaction of FICD's
387 TPR1 domain with a tripartite ATP state-specific Hsp70 surface composed of BiP's
388 NBD, linker and SBD β . Moreover, the TPR domain of FICD is only able to direct BiP's
389 $\ell_{7,8}$ SBD β region into the Fic domain active site when BiP's NBD and SBD are closely
390 opposed, as in the domain-docked ATP-state. These features explain the finding that
391 the client protein-bound ADP-state BiP is not a substrate for AMPylation⁴ and suggests
392 a facile mechanism for substrate-level regulation of BiP AMPylation — in which
393 substrate availability is inversely proportional to the unfolded protein load in the ER.

394 A reciprocal mechanism for substrate-level regulation of deAMPylation is unlikely, as
395 AMPylated BiP is intrinsically biased towards the ATP-like domain-docked state⁵.
396 Thus, evidence from biochemical and cell-based experiments for similar engagement
397 of BiP in FICD-mediated AMPylation and deAMPylation, suggests that regulatory
398 changes in FICD's active site contribute to the enzyme's ability to respond to changes
399 in the burden of ER unfolded proteins. Previous studies uncovered a role for a
400 monomerisation-induced increase in Glu234 flexibility, which permits AMPylation
401 competent binding of MgATP within the FICD active site²⁰. However, the basis for the
402 relationship between oligomeric state and deAMPylation activity remained obscure,
403 awaiting clarification of the enzymatic mechanism and the essential role played by
404 Glu234 in FICD-mediated deAMPylation.

405 The crystal structures presented in this work provide strong support for a mechanism
406 of eukaryotic deAMPylation that is acid-base in nature and in which Glu234 aligns a
407 catalytic water molecule in-line for nucleophilic attack into α -phosphate of Thr518-
408 AMP (**Supplementary Fig. 6**). Glu234, may act as a catalytic base but through a

409 mechanism involving late proton transfer analogous to the role played by the catalytic
410 aspartates of some protein kinases^{30,31}. This proposed deAMPylation mechanism
411 (which also rationalises the essential role for a divalent cations and His363) is far
412 removed from the binuclear metal-catalysed reactions catalysed by the other two known
413 (bacterial) deAMPylases^{21,24}. Moreover, other mechanisms of phosphodiester bond
414 cleavage, including anchimeric assistance or an E1cB-type elimination reaction, which
415 are capable of generating the products of FICD-mediated deAMPylation (AMP and
416 unmodified BiP), are rendered extremely unlikely by the structure of the deAMPylation
417 complex (**Supplementary Fig. 1b**).

418 A hydrolytic S_N2-type acid-base catalysed nucleophilic-substitution reaction,
419 facilitated by Glu234 and His363, represents a highly plausible deAMPylation
420 mechanism that is supported by the structure of the deAMPylation complex. As a
421 bacterial Fic protein (EffFic) has also been observed to possess gatekeeper glutamate-
422 dependent deAMPylation activity¹³, it is likely that the mechanism of deAMPylation
423 outlined above is conserved across this class of proteins. This conclusion, pertaining to
424 the immediate role of Glu234 in enabling BiP-AMP hydrolysis, permits various
425 inferences to be made about the role of monomerisation and increased Glu234
426 flexibility²⁰ in the regulation of deAMPylation activity. These, are supported by the
427 direct observation of a monomeric FICD-deAMPylation complex with an alternative
428 Glu234 conformation, resulting in a (state 2) deAMPylation non-competent active site
429 lacking a stably coordinated catalytic water molecule. Thus, increased Glu234
430 flexibility, induced by FICD monomerisation, not only considerably increases
431 AMPylation activity but also decreases the deAMPylation k_{cat} (**Fig. 6**).

432 Oligomeric-state changes in the disposition of the gatekeeper Glu234 may not be the
433 only mechanism for enzyme-based regulation of the BiP AMPylation-deAMPylation
434 cycle. Observations that monomeric FICD binds more tightly to unmodified BiP than
435 BiP-AMP and the converse being true for dimeric FICD, remain unexplained by the
436 structure of the FICD deAMPylation complex, suggesting that other factors may
437 contribute to regulation. For example, there may well be subtle differences in the
438 interactions between FICD and BiP mediated by changes in oligomeric
439 state/modification status or by FICD protein dynamics; as hinted at by the
440 crystallographic and SANS-based evidence for TPR domain flexibility and by the
441 effects of TPR fixation on enzyme-substrate complex formation and catalysis.

442 These caveats notwithstanding, this study advances our mechanistic understanding of
443 the reciprocal-regulation of enzymatic activity afforded by FICD's oligomerisation-
444 state dependent switch (**Fig. 6**). This leaves unanswered the question of how the FICD
445 monomer-dimer equilibrium responds to changing conditions in the ER. There is some
446 evidence that FICD may respond to the energy-status of the ER, as a proxy for ER
447 stress²⁰. Given that Hsp70 proteins can directly modulate the oligomeric status (and
448 thus activity) of their own regulators within the ER³² and cytosol/nucleus³³, the
449 possibility of an additional layer of BiP-driven FICD-regulation is therefore an
450 intriguing one to consider.

451

452 Materials and Methods

453

454 Plasmid construction

455 The plasmids used in this study have been described previously or were generated by
456 standard molecular cloning procedures and are listed in **Supplementary Table 2**.

457

458 Protein purification

459 All proteins were purified using the method for FICD protein expression detailed in²⁰,
460 with only minor modifications. In brief, proteins were expressed as N-terminal His₆-
461 Smt3 fusion constructs from either pET28-b vectors (expressed in T7 Express *lysY/I^q*
462 (NEB) *Escherichia coli* (*E. coli*) cells), or pQE30 vectors (expressed in M15 *E. coli*
463 cells (Qiagen)). T7 Express cells were grown in LB medium containing 50 µg/ml
464 kanamycin. M15 cells were grown in the same medium supplemented with an
465 additional 100 µg/ml ampicillin. All cells were grown at 37 °C to an optical density
466 (OD_{600nm}) of 0.6 and then shifted to 18 °C for 20 min, followed by induction of protein
467 expression with 0.5 mM isopropylthio β-D-1-galactopyranoside (IPTG). Cells were
468 harvested by centrifugation after a further 16 h at 18 °C.

469 Only the predicted structured regions of human FICD were expressed (residues 104–
470 445). For ‘full-length’ BiP constructs, that is to say constructs containing the complete
471 structured region of the SBD α lid subdomain, residues 27–635 of Chinese hamster BiP
472 were expressed. This excludes an unstructured acidic N-terminal region and the C-
473 terminal unstructured region bearing the KDEL. Note, in the recombinantly expressed
474 residue range hamster and human BiP are identical in terms of amino acid identity. For
475 use as an immobilised BLI ligand full-length BiP was expressed with an avi-tag inserted
476 C-terminal to Smt3 and N-terminal to a GS linker and hamster BiP residues 27–635.

477 All BiP constructs used in this study were made ATPase³⁴ and substrate-binding³⁵
478 deficient via introduction of Thr229Ala and Val461Phe mutations, respectively.
479 Thr229Ala allows BiP to bind and domain-dock in response to MgATP, even when
480 immobilised via an N-terminal biotinylated Avi-tag²⁰. The lack of ATP hydrolysis
481 enables BiP to remain bound to ATP in its domain-docked state for prolonged periods
482 of time, a feature which favours binding to²⁰ and AMPylation by FICD⁴. Both

483 Thr229Ala (in the presence of ATP) and Val461Phe (independent of nucleotide)
484 disfavour the binding of proteins within BiP's SBD (which principally occurs in the
485 apo or ADP-state).

486 Following harvesting and lysis of the bacterial pellets, proteins were purified through
487 the use of Ni-NTA agarose (Thermo Fisher), on-bead Ulp1 cleavage, anion exchange
488 and gel filtration chromatography as described in²⁰ with minor modifications. All
489 purification was conducted at 4 °C. Unless otherwise specified (below) anion exchanges
490 were conducted using a RESOURCE Q 6 ml column (GE Healthcare) with a linear
491 gradient ranging from 95% AEX-A (25 mM Tris-HCl pH 8.0) and 5% AEX-B (25 mM
492 Tris-HCl, 1 M NaCl) to 50% AEX-A and 50% AEX-B (see **Supplementary Table 2**).
493 Gel filtration was conducted, depending on protein size and amount, on either a HiLoad
494 16/60 Superdex 75 or 200 prep grade column or a S200 or S75 Increase 10/300 GL
495 column (see **Supplementary Table 2**). All proteins were purified to homogeneity and
496 > 95% purity, as assessed by Coomassie-stained SDS-PAGE. Unless the protein was
497 deliberately oxidised they were supplemented after gel filtration with 1 mM tris(2-
498 carboxyethyl)phosphine (TCEP). Proteins were concentrated to > 150 µM using
499 centrifugal filters (Amicon Ultra; Merck Millipore), aliquoted and snap-frozen and
500 stored at –80 °C. All protein concentrations were calculated using A₂₈₀, measured on a
501 NanoDrop One (Thermo Fisher), and the protein's predicted extinction coefficient at
502 280 nm (ε₂₈₀).

503 Preparative BiP AMPylation

504 In the case of preparative scale AMPylation of BiP, this was achieved post-Ulp1
505 cleavage by addition of 10 mM MgCl₂, 5 mM ATP and 1/50 (w/w) GST-TEV-
506 FICD^{E234G} (UK1479; purified as previously²⁰). The AMPylation reaction was incubated
507 for 16 h at 25 °C. GST-TEV-FICD was then depleted by a 1 h incubation with GSH-
508 Sepharose 4B matrix (GE Healthcare). AMPylation was confirmed as being
509 stoichiometric by intact-protein mass spectrometry (LC-ESI-MS) as previously
510 detailed⁵.

511 Disulphide-linked FICD dimers and BiP biotinylation

512 Disulphide-linked FICD dimers (s-sFICD^{A252C-H363A-C421S}; UK2269), used as a BiP-
513 AMP trap for in vitro AMPylation assays, were oxidised and purified as in a previous
514 study²⁰. Likewise, in vitro biotinylation of N-terminally avi-tagged BiP was conducted

515 and the proteins made apo and purified as previously described²⁰ with the exception
516 that ion-exchange fractions were diluted with glycerol and stored at -20 °C in a final
517 buffer of TNTG (12.5 mM Tris-HCl pH 8.0, ~ 150 mM NaCl, 0.5 mM TCEP and 50%
518 (v/v) glycerol), without additional gel filtration (see **Supplementary Table 2**).

519 FICD TPR domain oxidation

520 Purification of TPR domain oxidised (TPRox) FICD^{D160C-T183C-C421S}-derivative proteins
521 was achieved as above (for other FICDs), with the addition of an oxidation and clean-
522 up AEX step. Note, the cysteine free FICD^{C421S} mutation was previously observed to
523 have no effect on FICD-mediated deAMPylation or BiP-AMP binding and a slight
524 stimulatory effect on FICD-mediated AMPylation²⁰.

525 In order to form the disulphide-bond, the FICD protein (post-Ulp1 cleavage and Ni-
526 NTA column elution) was diluted down to a concentration of 5 µM in a final buffer of
527 25 mM Tris-HCl pH 8.0 and 100 mM NaCl, supplemented with 0.5 mM CuSO₄ and
528 1.75 mM 1,10-phenanthroline (Sigma), and incubated for 16 h at 4 °C. The oxidation
529 reaction was then quenched by the addition of 2 mM EDTA. The protein solution,
530 diluted with 25 mM Tris pH 8.0 to a final NaCl concentration of 50 mM, was then
531 purified on a HiTrap 5 ml Capto Q column (equilibrated in 95% AEX-A and 5% AEX-
532 B buffer) using a linear gradient of 5–50% AEX-B over 10 column volumes.
533 Proteinaceous fractions were further purified as detailed above (beginning with
534 RESOURCE Q column purification), culminating in the purification of dimeric or
535 monomeric FICD (as appropriate) by gel filtration.

536 Stoichiometric disulphide bond formation was confirmed by the use of an
537 electrophoretic mobility assay (see **Supplementary Fig. 3c**), in which the putatively
538 oxidised protein was heated for 10 min at 70 °C in SDS-Laemmli buffer ± DTT; all
539 available thiols were then reacted with a large excess of PEG 2000 maleimide (30 min
540 at 25 °C). All unreacted maleimides were then quenched by the addition of a molar
541 excess of DTT before samples were analysed by SDS-PAGE. Significant PEG
542 modification of FICD(TPRox) proteins was only observed in samples first denatured
543 in reducing conditions (+ DTT), suggesting that the two TPR domain-cysteines were
544 not accessible for alkylation in the absence of DTT (on account of being oxidised to
545 form an intramolecular disulphide bond).

546

547 **Protein crystallisation and structure determination**

548 Monomeric FICD^{L258D-H363A} (residues 104–445) [UK2093] and monomeric lid-
549 truncated BiP^{T229A-V461F}-AMP (residues 27–549) [UK2090] were purified as above and
550 gel filtered into a final buffer of T(10)NT (10 mM Tris-HCl pH 8.0, 150 mM NaCl and
551 1 mM TCEP). As outlined in the text, FICD's His363Ala mutation facilitates a stable
552 trapping of its deAMPylation substrate. As mentioned above, BiP^{T229A-V461F} favours its
553 monomeric ATP-state, in which it is less likely to bind substrates in its SBD and to
554 form BiP oligomers. The removal of all but helix A of the SBD α (BiP residues 27–549)
555 was also implemented to reduce the affinity of BiP substrate binding and
556 oligomerisation and to increase the likelihood of crystallisation and high resolution
557 diffraction by removal of the flexible SBD α helix B, which in other Hsp70s has been
558 documented to only transiently interact with the NBD in the ATP-state²⁸. Heterodimer
559 copurification was achieved by mixing FICD^{L258D-H363A} and BiP^{T229A-V461F}-AMP in a
560 1.5:1 molar ratio, supplemented with an additional 250 μ M ATP, 50 mM KCl and 2
561 mM MgCl₂. The mixture was incubated for 10 min at 4 °C and purified by gel filtration
562 on an S200 Increase 10/300 GL column equilibrated in TNKMT buffer (10 mM Tris-
563 HCl pH 8.0, 100 mM NaCl, 50 mM KCl, 2 mM MgCl₂ and 1 mM TCEP) with \leq 5 mg
564 of protein injected per SEC run. Heterodimeric protein fractions were pooled (as
565 indicated in **Fig. 1a**) and concentrated to 10.3 mg/ml using a 50 kDa MWCO centrifugal
566 filters.

567 Crystallisation solutions, consisting of 100 nl protein solution and 100 nl crystallisation
568 reservoir solution, were dispensed using a mosquito crystal (SPT Labtech) and the
569 complex was crystallised via sitting drop vapour diffusion at 25 °C. State 1 crystals
570 were obtained from reservoir conditions of 0.1 M MES pH 6.5, 10% PEG 4000 and 0.2
571 M NaCl; state 2 crystals were obtained from conditions of 0.1 M Tris pH 8.0 and 25%
572 PEG 400. Crystals were cryoprotected in a solution consisting of 25% glycerol and
573 75% of the respective reservoir solution (v/v).

574 Diffraction data were collected from the Diamond Light Source at 100 K (beamline
575 I04-1), and the data processed using DIALS³⁶ (state 1 crystal) or xia2³⁷ (state 2 crystal)
576 and the CCP4 module Aimless^{38,39}. Structures were solved by molecular replacement
577 using the CCP4 module Phaser^{38,40}. AMPylated BiP (PDB 5O4P) and monomeric FICD
578 (PDB 6I7L) structures from the Protein Data Bank were used as initial search models.
579 Manual model building was carried out in COOT⁴¹ and refined using refmac5⁴² with

580 TLS added. Metal binding sites were validated using the CheckMyMetal server⁴³.
581 Polder (OMIT) maps were generated using the Polder Map module of Phenix^{44,45}.
582 Structural figures were prepared using UCSF Chimera⁴⁶, estimates of interaction
583 surface areas were derived from PISA analysis⁴⁷, interaction maps (**Supplementary**
584 **Fig. 1**) were based on an initial output from LigPlot⁴⁸ and the chemical reaction
585 pathway (**Supplementary Fig. 6**) was created in ChemDraw (PerkinElmer
586 Informatics).

587

588 **Contrast Variation Small Angle Neutron Scattering**

589 Non-deuterated BiP^{T229A-V461F}-AMP (residues 27-635) and FICD^{H363A} (residues 104-
590 445) [hBiP-AMP and hFICD] were purified as detailed above but were gel filtered into
591 a final buffer of TNKMT(0.2) [TNKMT buffer with TCEP reduced to 0.2 mM]. The
592 matchout deuterium labelled protein equivalents were produced in the ILL's
593 deuteration laboratory (Grenoble, France). Proteins were expressed from *E. coli* BL21
594 Star (DE3) cells (Invitrogen) that were adapted to 85% deuterated Enfors minimal
595 media containing unlabelled glycerol as carbon source, as described previously^{49,50}, in
596 the presence of kanamycin at a final concentration of 35 µg/ml. The temperatures at
597 which the cells produced the highest amount of soluble matchout-deuterated BiP or
598 FICD were chosen for cell growth using a high cell density fermentation process in a
599 bioreactor (Labfors, Infors HT). For BiP expression, cells were grown using a fed-batch
600 fermentation strategy at 30 °C to an OD₆₀₀ of 20. The temperature was then decreased
601 to 18 °C and protein expression was induced by addition of 1 mM IPTG. After a further
602 22 h of protein expression at 18 °C, bacteria were harvested by centrifugation. FICD
603 expression was conducted likewise, but with induction at OD₆₀₀ 19 and at a temperature
604 of 22 °C. FICD expressing cells were incubated for a further 21.5 h at 22 °C before
605 harvesting. Matchout-deuterated proteins (dBiP^{T229A-V461F}-AMP and dFICD^{H363A}) were
606 isolated and purified from deuterated cell pastes using H₂O-based buffer systems, as
607 mentioned above, and gel filtered into TNKMT(0.2).

608 Heterotetrameric complexes were copurified by gel filtration of a mixture of either
609 dBiP-AMP and hFICD or hBiP-AMP and dFICD (in a 1.25:1 molar ratio of BiP-
610 AMP:FICD), with ≤ 5 mg of protein injected per SEC run, supplemented with 250 µM
611 ATP. The gel filtration was conducted on an S200 Increase 10/300 GL column

612 equilibrated with TNKMT(0.2) buffer. Heterotetrameric complex fractions were
613 collected and concentrated to > 7 mg/ml. Some of this purified complex was further
614 exchanged by the same SEC process into TNKMT(0.2) in which the solvent used was
615 D₂O. That is to say, the complex was exchanged into 100% D₂O buffer. Protein
616 fractions in 100% D₂O buffer were subsequently concentrated to > 6 mg/ml. The elution
617 profile appeared largely identical in both deuterated and non-deuterated buffers.
618 Complexes at different %D₂O were obtained by either dilution with the appropriate
619 matched buffer (\pm D₂O) or by the mixing of one complex purified in 0% D₂O buffer
620 with the same complex in 100% D₂O buffer.

621 SANS data were collected from a total of 17 samples at various D₂O buffer
622 compositions at 12 °C at the ILL beamline D11. Protein complexes (ranging from 4.3
623 to 5.5 mg/ml) were analysed in a 2 mm path-length quartz cell with a 5.5 Å wavelength
624 neutron beam at distances of 1.4, 8 and 20.5 m. Data from relevant buffer-only controls
625 were also collected with similar data collection times and subtracted from the radially
626 averaged sample scattering intensities to produce the $I(q)$ against q scattering curves
627 presented in **Fig. 2a**. Scattering data were initially processed with the GRASP
628 (Graphical Reduction and Analysis SANS Program for Matlab; developed by Charles
629 Dewhurst, ILL) and with the Igor Pro software (WaveMetrics) using SANS macros⁵¹.
630 Data analysis was conducted using Prism 8.4 (GraphPad) and PEPSI-SANS (for fitting
631 of theoretical scattering curves and flex-fit model generation; software based on PEPSI-
632 SAXS⁵²).

633 Comparison of the $\ln(\text{Transmission})$ of the 0% and 100% D₂O buffers alone with the
634 $\ln(\text{Transmission})$ of each sample (not shown) confirmed that the %D₂O of each sample
635 was within the margin of error of the theoretical D₂O content⁵³.

636 Parameters from the Guinier plots were derived from fitting of the Guinier
637 approximation⁵⁴:

$$638 \quad \ln(I(q)) = \ln(I(0)) - \frac{R_g^2}{3} q^2$$

639 The upper and lower q limits for fitting are shown (grey vertical dashed lines in **Fig. 2b**
640 and **Supplementary Fig. 2a**, except for the fitting of hFICD•dBiP-AMP in 60% D₂O
641 buffer where the lower q limit is denoted by purple vertical dashed line) and result in

642 $qR_g < 1.3$ (with the exception of the fitting of dFICD•hBiP-AMP in 80% D₂O buffer
643 data where $qR_g = 1.4$).

644 The contrast match point analysis (CMP) in **Fig. 2c** indicated complex match points of
645 76.7% D₂O (95% CI: 71.5 to 82.4% D₂O) and 61.4 D₂O (95% CI: 57.4 to 65.5% D₂O)
646 for hFICD•dBiP-AMP and dFICD•hBiP-AMP, respectively. Comparison of the
647 experimental CMPs with theoretical values calculated by MULCh⁵⁵ (which takes into
648 account buffer composition effects (at 20 °C) and protein sequence, whilst assuming a
649 1:1 complex and 95% labile H/D-exchange) suggested that there was 66.5% deuteration
650 of dBiP-AMP and a 63.8% deuteration of dFICD. Note, these deuteration values are
651 less than the theoretical maximum which could have been obtained from the 85%
652 deuterated *E. coli* growth media, see above. These values of (non-labile) protein
653 (partial) deuteration were used to calculate theoretical $I(0)/c$ values in SASSIE⁵⁶, using
654 the same assumptions as above. Comparison of the theoretical $I(0)/c$ values with those
655 determined from the experimental Guinier analysis facilitated experimental protein-
656 complex MW estimation⁵⁷ (**Supplementary Table 1**). The contrast at each %D₂O (the
657 difference in scattering length density (SLD), $\Delta\rho$, between the ρ_{protein} and ρ_{buffer}) was
658 also derived from MULCh.

659 Stuhrmann analysis was carried out by the fitting of the relationship²⁷:

660
$$R_g^2 = R_m^2 + \frac{\alpha}{\Delta\rho} - \frac{\beta}{\Delta\rho^2}$$

661 In which R_m^2 represent the R_g if it were to have a homogenous SLD. The value of α
662 reflects the radial distribution of SLD, with values > 0 suggesting that higher contrast
663 components are located towards the outside of the complex. The value of β is a
664 reflection of the distance of the centre of the complex's SLD from the complex's centre
665 of mass. In the case of the Stuhrmann plot of dFICD•hBiP-AMP a linear best-fit line
666 (suggesting $\beta \approx 0$) was a considerably better fit to the data (shown in **Fig. 2d**; $R^2 = 0.93$)
667 than the fitting of a quadratic curve ($R^2 = 0.66$). Theoretical R_g values, derived from
668 structural models, were calculated using CRYSON⁵⁸. The symmetry of structural
669 models was assessed through the use of AnAnaS software⁵⁹.

670

671 **Differential Scanning Fluorimetry (DSF)**

672 DSF experiments were performed on a CFX96 Touch Real-Time PCR Detection
673 System (Bio-Rad) in 96-well plates (Hard-Shell, Bio-Rad) sealed with optically clear
674 Microseal 'B' Adhesive Sealer (Bio-Rad). Each sample was measured in technical
675 duplicate and in a final volume of 20 μ l. Protein was used at a final concentration of 2
676 μ M, ATP or ADP (if applicable) at 5 and 2 mM, respectively, and SYPRO Orange dye
677 (Thermo Fisher) at a 10 \times concentration in a buffer of HKM (25 mM HEPES-KOH pH
678 7.4, 150 mM KCl, 10 mM MgCl₂). Solutions were briefly mixed and the plate spun at
679 200 g for 10 s before DSF measurement. Fluorescence of the SYPRO Orange dye was
680 monitored on the FRET channel over a temperature range of 25–90 °C with 0.5 °C
681 intervals. Background fluorescence changes were calculated and subtracted from the
682 protein sample fluorescence data using no-protein control (NPC) wells. NPC
683 fluorescence was unchanged by the addition of ATP or ADP. Data was then analysed
684 in Prism 8.4 (GraphPad), with melting temperatures calculated as the global minimums
685 of the negative first derivatives of the relative fluorescent unit (RFU) melt curves (with
686 respect to temperature).

687

688 **Bio-layer interferometry (BLI)**

689 AMPylated or non-AMPylated biotinylated-AviTag-haBiP^{T229A-V461F} (UK2359), was
690 AMPylated if applicable, in vitro biotinylated (as previously described²⁰), made apo
691 and purified as detailed above in *Protein Purification*. Both proteins were confirmed as
692 being > 95% biotinylated by streptavidin gel-shift. All BLI experiments were
693 conducted on the FortéBio Octet RED96 System (Pall FortéBio) using in a buffer basis
694 of HKM supplemented with 0.05% Triton X-100 (HKMTx). Streptavidin (SA)-coated
695 biosensors (Pall FortéBio) were hydrated in HKMTx for at least 30 min at 25 °C prior
696 to use. Experiments were conducted at 30 °C. BLI reactions were prepared in 200 μ l
697 volumes in 96-well microplates (greiner bio-one). Ligand loading was performed with
698 biotinylated BiP-AMP:Apo at 7.5 nM and with biotinylated BiP:Apo at 5.8 nM, such
699 that the rate of ligand loading was roughly equivalent and all tips reached a threshold
700 of 1 nm binding signal (displacement) within 300–600 s. All ligands loaded with a
701 range of 1.0–1.2 nm. After loading of the immobilised ligand, BiP was activated in 2
702 mM ATP for 200 s, followed by a 50 s baseline in HKMTx alone, before association
703 with apo FICD variants (all bearing a catalytically inactivating His363Ala mutation and
704 at 50 nM unless otherwise specified) in HKMTx (see schematic in **Supplementary Fig.**

705 **3d).** Note, immobilised (unmodified) BiP was previously observed to domain-dock,
706 and remain domain-docked for extended periods of time in ATP-replete buffer,
707 following this protocol of ATP activation²⁰. The first dissociation step was initiated by
708 the dipping of all tips into wells lacking FICD analyte (only HKMTx). The second
709 dissociation step was induced by the dipping of the biosensor tips into HKMTx
710 supplemented with 2 mM ATP. Experiments were conducted at a 1000 rpm shake speed
711 and with a 5 Hz acquisition rate. Data were processed in Prism 8.4 (GraphPad).

712

713 **In vitro deAMPylation (fluorescence polarisation) assay**

714 Measurement of deAMPylation kinetics was performed as described previously¹¹ with
715 modifications. The probe BiP^{T229A-V461F} (UK2521) modified with FAM-labelled AMP:
716 BiP^{T229A-V461F}-AMP(FAM)) was generated by pre-incubating 100 μ M apo BiP^{T229A-}
717 ^{V461F} with 5 μ M GST-FICD^{E234G} (UK1479) and 110 μ M ATP in HKM buffer for 5 min
718 at 20 °C, followed by addition of 100 μ M ATP-FAM [N⁶-(6-Amino)hexyl-ATP-6-
719 FAM; Jena Bioscience] and further incubation for 19 h at 25 °C. To ensure complete
720 BiP AMPylation 2 mM ATP was then added to the reaction which was incubated for a
721 further 1.25 h at 25 °C. The reaction mixture was then incubated with GSH-Sepharose
722 4B matrix for 45 min at 4 °C in order to deplete the GST-FICD^{E234G}. The BiP containing
723 supernatant was buffered exchanged into HKM using a Zeba Spin desalting column
724 (7K MWCO, 0.5 ml; Thermo Fisher) in order to remove the majority of free (FAM
725 labelled) nucleotide. 2 mM ATP was added to the eluted protein and incubated for 15
726 min at 4 °C (to facilitate displacement of any residual FAM-labelled nucleotide
727 derivates bound by the NBD of BiP). Pure BiP-AMP(FAM) with BiP-AMP was then
728 obtained by gel filtration using an S75 Increase 10/300 GL column equilibrated in
729 HKM at 4 °C. 1 mM TCEP was added to the protein fractions, which were concentrated
730 using a 50K MWCO centrifugal filter and snap frozen. A labelling efficiency of 1.8%
731 was estimated based on the extinction coefficient for BiP-AMP:ATP (ϵ_{280} 33.5 mM⁻¹
732 cm⁻¹), FAM (ϵ_{492} 83.0 mM⁻¹ cm⁻¹) and a 280/492 nm correction factor of 0.3 (Jenna
733 Biosciences).

734 DeAMPylation reactions were performed in HKMTx(0.1) buffer [HKM supplemented
735 with 0.1% (v/v) Triton X-100] in 384-well polysterene microplates (black, flat bottom,
736 μ CLEAR; greiner bio-one) at 30 °C in a final volume of 30 μ l containing trace amounts

737 of fluorescent BiP^{T229A-V461F}-AMP(FAM) probe (10 nM), supplemented with BiP^{T229A-}
738 ^{V461F}-AMP (5 μ M) and FICD proteins (0.5 μ M). A well lacking FICD protein was used
739 for baseline FP background subtraction. 10 nM ATP-FAM alone was also included as
740 a low FP control (not shown). Under these conditions $[E]_0$ was assumed to be $\ll [S]_0$
741 + K_M (with $[E]_0 = 0.5 \mu$ M, $[S]_0 = 5 \mu$ M and the presumed K_M (Michaelis constant) \geq
742 GST-FICD K_M of 16 μ M¹¹) such that quasi-steady state reaction kinetics should apply
743 with respect to the initial reaction rate. Furthermore, $[S]_0$ was considered to be
744 sufficiently small relative to the FICD variant presumed K_M values such that, by
745 derivation from the Michaelis-Menten equation⁶⁰, the following relationship holds true:

746

$$v \approx \frac{k_{cat}}{K_M} [E]_0 [S]_0$$

747 where v is the measured initial reaction velocity. On account of the close
748 correspondence between the values calculated here and previously (from a Michaelis-
749 Menten analysis of GST-FICD¹¹) these assumptions are clearly valid for wild type
750 FICD. More accurately all presented $\sim k_{cat}/K_M$ values are in fact equivalent to $k_{cat}/(K_M$
751 + $[S]_0)$.

752 Fluorescence polarisation of FAM ($\lambda_{ex} = 485$ nm, $\lambda_{em} = 535$ nm) was measured with an
753 Infinite F500 plate reader (Tecan). The mFP y_0 difference between the FICD^{L258D} time
754 course and the same reaction composition pre-incubated for 5 h at 25 °C before the
755 beginning of data collection, was interpreted as the Δ mFP equivalent to complete (5
756 μ M) BiP-AMP deAMPylation (see **Supplementary Fig. 3e**). Fitting of the initial linear
757 reaction phase was achieved using Prism 8.4 (GraphPad).

758 For direct calculation of k_{cat} values deAMPylation assays were conducted as above but
759 with 10 μ M FICD or FICD^{L258D} and 100 or 150 μ M BiP-AMP substrate. Following
760 subtraction of a no enzyme background from all datasets, the mFP difference for each
761 sample (between $t = 0$ and the mFP plateau) was interpreted as the Δ mFP equivalent to
762 complete BiP-AMP deAMPylation ($[S]_0$).

763

764 **In vitro AMPylation**

765 In vitro AMPylation reactions were performed in HKM buffer in a 7 μ l volume.
766 Reactions contained 10 μ M ATP-FAM, 5 μ M ATP-hydrolysis and substrate-binding
767 deficient BiP^{T229A-V461F} (UK2521), 7.5 μ M oxidised s-sFICD^{A252C-H363A-C421S} (UK2269,

768 trap) to sequester any modified BiP [BiP-AMP(FAM)] and, unless otherwise stated, 0.5
769 μ M FICD. Reactions were started by addition of nucleotide. Apart from in the presented
770 time courses (**Supplementary Fig. 4b**) after a 60 min incubation at 25 °C the reactions
771 were stopped by addition of 3 μ l 3.3 \times LDS sample buffer (Sigma) containing NEM
772 (40 mM final concentration) for non-reducing SDS-PAGE or DTT (50 mM final
773 concentration) for reducing SDS-PAGE and heated for 10 min at 70 °C. Samples were
774 applied to a 10% SDS-PAGE gel, the FAM-label was imaged with a Chemidoc MP
775 (Bio-Rad) using the Alexa Flour 488 dye setting. Gels were subsequently stained with
776 Quick Coomassie (Neo Biotech).

777

778 **Mammalian Cell Culture and Lysis**

779 The CHO-K1 *FICD*^{-/-} cell line used in this study was described previously⁴. The CHO-
780 K1 S21 *FICD*^{-/-} cell line was generated by CRISPR-Cas9 knockout of both FICD
781 alleles (as described previously⁴) into the previously described UPR reporter
782 *CHOP::GFP* and *XBPIs::Turquoise* bearing CHO-K1 S21 cell line⁶¹. Cells were
783 cultured as in²⁰. Where indicated, cells were treated for 3 h with cycloheximide (Sigma)
784 by exchanging the culture medium with pre-warmed (37 °C) medium supplemented
785 with cycloheximide at 100 μ g/ml. Cell lysates were obtained and analysed as in²⁰ but
786 with a HG lysis buffer consisting of 20 mM HEPES-KOH pH 7.4, 150 mM NaCl, 2
787 mM MgCl₂, 33 mM D-glucose, 10% (v/v) glycerol, 1% (v/v) Triton X-100 and protease
788 inhibitors (2 mM phenylmethylsulphonyl fluoride (PMSF), 4 μ g/ml pepstatin, 4 μ g/ml
789 leupeptin, 8 μ g/ml aprotinin) with 100 U/ml hexokinase (from *Saccharomyces*
790 *cerevisiae* Type F-300; Sigma).

791

792 **Immunoblot (IB) analysis**

793 After separation by SDS-PAGE or native-PAGE (as previously described²⁰) proteins
794 were transferred onto PVDF membranes. The membranes were blocked with 5% (w/v)
795 dried skimmed milk in TBS (25 mM Tris-HCl pH 7.5, 150 mM NaCl) and incubated
796 with primary antibodies followed by IRDye fluorescently labelled secondary antibodies
797 (LI-COR). The membranes were scanned with an Odyssey near-infrared imager (LI-
798 COR). Primary antibodies and antisera against hamster BiP [chicken anti-BiP⁶²], eIF2 α
799 [mouse anti-eIF2 α ⁶³] and FICD [chicken anti-FICD⁴] were used.

800

801 **Flow cytometry**

802 FICD over-expression-dependent induction of unfolded protein response signalling
803 was analysed by transient transfection of CHO-K1 S21 *FICD*^{-/-} UPR reporter cell lines
804 with plasmid DNA encoding the complete FICD coding sequence (with mutations as
805 indicated) and mCherry as a transfection marker, using Lipofectamine LTX (Thermo
806 Fisher) as described previously⁴. 0.5 µg DNA was used to transfect cells growing in
807 12-well plates. 40 h after transfection the cells were washed with PBS and collected in
808 PBS containing 4 mM EDTA, and single live-cell fluorescent signals (20,000 collected
809 per sample) were analysed by dual-channel flow cytometry with an LSRFortessa cell
810 analyser (BD Biosciences). Turquoise and mCherry fluorescence was detected using a
811 405 nm excitation laser with a 450/50 nm emission filter and a 561 nm excitation laser
812 with a 610/20 nm emission filter, respectively. Data were processed using FlowJo and
813 the extracted population parameters were plotted in Prism 8.4 (GraphPad).

814

815 **Data availability**

816 The deAMPylation complex crystal structures of monomeric FICD and AMPylated BiP
817 have been deposited in the Protein Data Bank (PDB) with the following accession
818 codes: 7B7Z (State 1), 7B80 (State 2). Raw SANS data is available from
819 doi:10.5291/ILL-DATA.8-03-963.

820

821 **Acknowledgements**

822 We thank the Huntington lab for access to the Octet machine and the CIMR flow
823 cytometry core facility team (Reiner Schulte, Chiara Cossetti and Gabriela Grondys-
824 Kotarba). This work was supported by Wellcome Trust Principal Research Fellowship
825 to D.R. (Wellcome 200848/Z/16/Z), and a Wellcome Trust Strategic Award to the
826 Cambridge Institute for Medical Research (Wellcome 100140). We are grateful to the
827 Diamond Light Source for X-ray beamtime (proposal MX-21426) and the staff of
828 beamline I04-1 for assistance with data collection; and to the ILL for neutron beamtime
829 as part of proposal 8-03-963 with particular thanks to Anne Martel for her assistance.
830 For advice pertaining to the use of PEPSI-SANS software we thank Sergei Grudinin.
831 We are indebted to Yahui Yan for the gift of FICD's TPR domain-expressing plasmid
832 and to Cláudia Rato da Silva for advice and guidance on the in vivo experiments. We
833 also thank Yahui Yan, Alisa F. Zyryanova and Lisa Neidhardt for comments on the
834 manuscript.

835

836 **Author contributions**

837 L.A.P. led and conceived the project, designed and conducted the experiments,
838 analysed and interpreted all the data, purified and crystallised proteins, collected,
839 analysed and interpreted the X-ray diffraction and neutron scattering data, and wrote
840 the manuscript. S.P.¹ conducted the FP assays, purified proteins. N.Z. and S.P.² helped
841 to collect and process scattering data. J.M.D. and M.H. expressed the deuterated
842 proteins. All authors contributed to revising the article. D.R. conceived and oversaw
843 the project, interpreted the data, and wrote the manuscript.

844

845 **Conflict of interests**

846 The authors declare no conflict of interests.

847 **References**

848

- 849 1. Bakunts, A. *et al.* Ratiometric sensing of BiP-client versus BiP levels by the
850 unfolded protein response determines its signaling amplitude. *Elife* **6**, (2017).
- 851 2. Walter, P. & Ron, D. The unfolded protein response: from stress pathway to
852 homeostatic regulation. *Science* **334**, 1081–6 (2011).
- 853 3. Preissler, S. & Ron, D. Early Events in the Endoplasmic Reticulum Unfolded
854 Protein Response. *Cold Spring Harb. Perspect. Biol.* **11**, a033894 (2019).
- 855 4. Preissler, S. *et al.* AMPylation matches BiP activity to client protein load in the
856 endoplasmic reticulum. *Elife* **4**, e12621 (2015).
- 857 5. Preissler, S. *et al.* AMPylation targets the rate-limiting step of BiP's ATPase
858 cycle for its functional inactivation. *Elife* **6**, e29428 (2017).
- 859 6. Wieteska, L., Shahidi, S. & Zhuravleva, A. Allosteric fine-tuning of the
860 conformational equilibrium poises the chaperone BiP for post-translational
861 regulation. *Elife* **6**, e29430 (2017).
- 862 7. Laitusis, A. L., Brostrom, M. A. & Brostrom, C. O. The dynamic role of
863 GRP78/BiP in the coordination of mRNA translation with protein processing.
864 *J. Biol. Chem.* **274**, 486–493 (1999).
- 865 8. Chambers, J. E., Petrova, K., Tomba, G., Vendruscolo, M. & Ron, D. ADP
866 ribosylation adapts an ER chaperone response to short-term fluctuations in
867 unfolded protein load. *J. Cell Biol.* **198**, 371–85 (2012).
- 868 9. Ham, H. *et al.* Unfolded protein response-regulated Drosophila Fic (dFic)
869 protein reversibly AMPylates BiP chaperone during endoplasmic reticulum
870 homeostasis. *J. Biol. Chem.* **289**, 36059–69 (2014).
- 871 10. Sanyal, A. *et al.* A Novel Link between Fic (Filamentation Induced by cAMP)-
872 mediated Adenylylation/AMPylation and the Unfolded Protein Response. *J.*
873 *Biol. Chem.* **290**, 8482–8499 (2015).
- 874 11. Preissler, S., Rato, C., Perera, L., Saudek, V. & Ron, D. FICD acts
875 bifunctionally to AMPylate and de-AMPylate the endoplasmic reticulum
876 chaperone BiP. *Nat. Struct. Mol. Biol.* **24**, 23–29 (2017).

877 12. Casey, A. K. *et al.* Fic-mediated deAMPylation is not dependent on homo-
878 dimerization and rescues toxic AMPylation in flies. *J. Biol. Chem.*
879 jbc.M117.799296 (2017). doi:10.1074/jbc.M117.799296

880 13. Veyron, S. *et al.* A Ca $^{2+}$ -regulated deAMPylation switch in human and
881 bacterial FIC proteins. *Nat. Commun.* **10**, 1142 (2019).

882 14. Khater, S. & Mohanty, D. In silico identification of AMPylating enzymes and
883 study of their divergent evolution. *Sci. Rep.* **5**, 10804 (2015).

884 15. Luong, P. *et al.* Kinetic and structural insights into the mechanism of
885 AMPylation by VopS Fic domain. *J. Biol. Chem.* **285**, 20155–63 (2010).

886 16. Xiao, J., Worby, C. A., Mattoo, S., Sankaran, B. & Dixon, J. E. Structural basis
887 of Fic-mediated adenylylation. *Nat. Struct. Mol. Biol.* **17**, 1004–10 (2010).

888 17. Khater, S. & Mohanty, D. Deciphering the Molecular Basis of Functional
889 Divergence in AMPylating Enzymes by Molecular Dynamics Simulations and
890 Structure Guided Phylogeny. *Biochemistry* **54**, 5209–24 (2015).

891 18. Engel, P. *et al.* Adenylylation control by intra- or intermolecular active-site
892 obstruction in Fic proteins. *Nature* **482**, 107–10 (2012).

893 19. Goepfert, A., Stanger, F. V., Dehio, C. & Schirmer, T. Conserved Inhibitory
894 Mechanism and Competent ATP Binding Mode for Adenylyltransferases with
895 Fic Fold. *PLoS One* **8**, e64901 (2013).

896 20. Perera, L. A. *et al.* An oligomeric state-dependent switch in the ER enzyme
897 FICD regulates AMPylation and deAMPylation of BiP. *EMBO J.* **38**, e102177
898 (2019).

899 21. Chen, Y. *et al.* Structural basis for Rab1 de-AMPylation by the Legionella
900 pneumophila effector SidD. *PLoS Pathog.* **9**, e1003382 (2013).

901 22. Anderson, W. B. & Stadtman, E. R. Glutamine synthetase deadenylylation: A
902 phosphorolytic reaction yielding ADP as nucleotide product. *Biochem.
903 Biophys. Res. Commun.* **41**, 704–709 (1970).

904 23. Xu, Y. *et al.* Structure of the N-terminal domain of Escherichia coli glutamine
905 synthetase adenylyltransferase. *Structure* **12**, 861–9 (2004).

906 24. Xu, Y., Carr, P. D., Vasudevan, S. G. & Ollis, D. L. Structure of the

907 adenylylation domain of *E. coli* glutamine synthetase adenylyl transferase:
908 evidence for gene duplication and evolution of a new active site. *J. Mol. Biol.*
909 **396**, 773–84 (2010).

910 25. Bunney, T. D. *et al.* Crystal structure of the human, FIC-domain containing
911 protein HYPE and implications for its functions. *Structure* **22**, 1831–43 (2014).

912 26. Worby, C. A. *et al.* The fic domain: regulation of cell signaling by
913 adenylylation. *Mol. Cell* **34**, 93–103 (2009).

914 27. Ibel, K. & Stuhrmann, H. B. Comparison of neutron and X-ray scattering of
915 dilute myoglobin solutions. *J. Mol. Biol.* **93**, 255–265 (1975).

916 28. Zhuravleva, A., Clerico, E. M. & Giersch, L. M. An Interdomain Energetic
917 Tug-of-War Creates the Allosterically Active State in Hsp70 Molecular
918 Chaperones. *Cell* **151**, 1296–1307 (2012).

919 29. Marcinowski, M. *et al.* Substrate discrimination of the chaperone BiP by
920 autonomous and cochaperone-regulated conformational transitions. *Nat. Struct.
921 Mol. Biol.* **18**, 150–158 (2011).

922 30. Valiev, M., Kawai, R., Adams, J. A. & Weare, J. H. The role of the putative
923 catalytic base in the phosphoryl transfer reaction in a protein kinase: First-
924 principles calculations. *J. Am. Chem. Soc.* **125**, 9926–9927 (2003).

925 31. Cheng, Y., Zhang, Y. & McCammon, J. A. How does the cAMP-dependent
926 protein kinase catalyze the phosphorylation reaction: An ab Initio QM/MM
927 study. *J. Am. Chem. Soc.* **127**, 1553–1562 (2005).

928 32. Amin-Wetzel, N., Neidhardt, L., Yan, Y., Mayer, M. P. & Ron, D.
929 Unstructured regions in IRE1 α specify BiP-mediated destabilisation of the
930 luminal domain dimer and repression of the UPR. *Elife* **8**, 1–35 (2019).

931 33. Kmiecik, S. W., Le Breton, L. & Mayer, M. P. Feedback regulation of heat
932 shock factor 1 (Hsf1) activity by Hsp70-mediated trimer unzipping and
933 dissociation from DNA. *EMBO J.* **39**, (2020).

934 34. Gaut, J. R. & Hendershot, L. M. Mutations within the nucleotide binding site of
935 immunoglobulin-binding protein inhibit ATPase activity and interfere with
936 release of immunoglobulin heavy chain. *J. Biol. Chem.* **268**, 7248–55 (1993).

937 35. Petrova, K., Oyadomari, S., Hendershot, L. M. & Ron, D. Regulated
938 association of misfolded endoplasmic reticulum luminal proteins with
939 P58/DNAJc3. *EMBO J.* **27**, 2862–72 (2008).

940 36. Beilsten-Edmands, J. *et al.* Scaling diffraction data in the DIALS software
941 package: Algorithms and new approaches for multi-crystal scaling. *Acta
942 Crystallogr. Sect. D Struct. Biol.* **76**, 385–399 (2020).

943 37. Winter, G. Xia2: An expert system for macromolecular crystallography data
944 reduction. *J. Appl. Crystallogr.* **43**, 186–190 (2010).

945 38. Winn, M. D. *et al.* Overview of the CCP4 suite and current developments. *Acta
946 Crystallogr. D. Biol. Crystallogr.* **67**, 235–42 (2011).

947 39. Evans, P. R. & Murshudov, G. N. How good are my data and what is the
948 resolution? *Acta Crystallogr. D. Biol. Crystallogr.* **69**, 1204–14 (2013).

949 40. McCoy, A. J. *et al.* Phaser crystallographic software. *J. Appl. Crystallogr.* **40**,
950 658–674 (2007).

951 41. Emsley, P., Lohkamp, B., Scott, W. G. & Cowtan, K. Features and
952 development of Coot. *Acta Crystallogr. Sect. D Biol. Crystallogr.* **66**, 486–501
953 (2010).

954 42. Winn, M. D., Murshudov, G. N. & Papiz, M. Z. Macromolecular TLS
955 Refinement in REFMAC at Moderate Resolutions. *Methods Enzymol.* **374**,
956 300–321 (2003).

957 43. Zheng, H. *et al.* CheckMyMetal : a macromolecular metal-binding validation
958 tool. *Acta Crystallogr. Sect. D Struct. Biol.* **73**, 223–233 (2017).

959 44. Liebschner, D. *et al.* Polder maps: improving OMIT maps by excluding bulk
960 solvent. *Acta Crystallogr. Sect. D Struct. Biol.* **73**, 148–157 (2017).

961 45. Adams, P. D. *et al.* PHENIX: a comprehensive Python-based system for
962 macromolecular structure solution. *Acta Crystallogr. D. Biol. Crystallogr.* **66**,
963 213–21 (2010).

964 46. Pettersen, E. F. *et al.* UCSF Chimera - A visualization system for exploratory
965 research and analysis. *J. Comput. Chem.* **25**, 1605–1612 (2004).

966 47. Krissinel, E. & Henrick, K. Inference of Macromolecular Assemblies from

967 48. Crystalline State. *J. Mol. Biol.* **372**, 774–797 (2007).

968 48. Laskowski, R. A. & Swindells, M. B. LigPlot+: Multiple ligand-protein
969 interaction diagrams for drug discovery. *J. Chem. Inf. Model.* **51**, 2778–2786
970 (2011).

971 49. Haertlein, M. *et al.* Biomolecular Deuteration for Neutron Structural Biology
972 and Dynamics. in *Methods in Enzymology* **566**, 113–157 (Academic Press Inc.,
973 2016).

974 50. Dunne, O. *et al.* Matchout deuterium labelling of proteins for small-angle
975 neutron scattering studies using prokaryotic and eukaryotic expression systems
976 and high cell-density cultures. *Eur. Biophys. J.* **46**, 425–432 (2017).

977 51. Kline, S. R. Reduction and analysis of SANS and USANS data using IGOR
978 Pro. *J. Appl. Crystallogr.* **39**, 895–900 (2006).

979 52. Grudinin, S., Garkavenko, M. & Kazennov, A. *Pepsi-SAXS* : an adaptive
980 method for rapid and accurate computation of small-angle X-ray scattering
981 profiles. *Acta Crystallogr. Sect. D Struct. Biol.* **73**, 449–464 (2017).

982 53. Zaccaï, G. Straight lines of neutron scattering in biology: A review of basic
983 controls in SANS and EINS. *European Biophysics Journal* **41**, 781–787
984 (2012).

985 54. Guinier, A. & Fournet, G. *Small-angle scattering of X-rays (Translation by C.*
986 *B. Walker)*. New York: Wiley; London: Chapman and Hall (New York: Wiley;
987 London: Chapman and Hall, 1955).

988 55. Whitten, A. E., Cai, S. & Trehewella, J. MULCh: Modules for the analysis of
989 small-angle neutron contrast variation data from biomolecular assemblies. *J.*
990 *Appl. Crystallogr.* **41**, 222–226 (2008).

991 56. Curtis, J. E., Raghunandan, S., Nanda, H. & Krueger, S. SASSIE: A program
992 to study intrinsically disordered biological molecules and macromolecular
993 ensembles using experimental scattering restraints. *Comput. Phys. Commun.*
994 **183**, 382–389 (2012).

995 57. Zaccaï, N. R. *et al.* Deuterium Labeling Together with Contrast Variation
996 Small-Angle Neutron Scattering Suggests How Skp Captures and Releases
997 Unfolded Outer Membrane Proteins. in *Methods in Enzymology* **566**, 159–210

998 (Academic Press, 2016).

999 58. Svergun, D. I. *et al.* Protein hydration in solution: Experimental observation by
1000 x-ray and neutron scattering. *Proc. Natl. Acad. Sci. U. S. A.* **95**, 2267–2272
1001 (1998).

1002 59. Pagès, G. & Grudinin, S. AnAnaS: Software for Analytical Analysis of
1003 Symmetries in Protein Structures. in *Methods in Molecular Biology* **2165**, 245–
1004 257 (Humana Press Inc., 2020).

1005 60. Michaelis, L., Menten, M. L., Johnson, K. A. & Goody, R. S. The original
1006 Michaelis constant: translation of the 1913 Michaelis-Menten paper.
1007 *Biochemistry* **50**, 8264–9 (2011).

1008 61. Sekine, Y. *et al.* Paradoxical Sensitivity to an Integrated Stress Response
1009 Blocking Mutation in Vanishing White Matter Cells. *PLoS One* **11**, e0166278
1010 (2016).

1011 62. Avezov, E. *et al.* Lifetime imaging of a fluorescent protein sensor reveals
1012 surprising stability of ER thiol redox. *J. Cell Biol.* **201**, 337–49 (2013).

1013 63. Scorsone, K. A., Panniers, R., Rowlands, A. G. & Henshaw, E. C.
1014 Phosphorylation of eukaryotic initiation factor 2 during physiological stresses
1015 which affect protein synthesis. *J. Biol. Chem.* **262**, 14538–43 (1987).

1016

1017

1018

1019 **Figure legends and Tables**

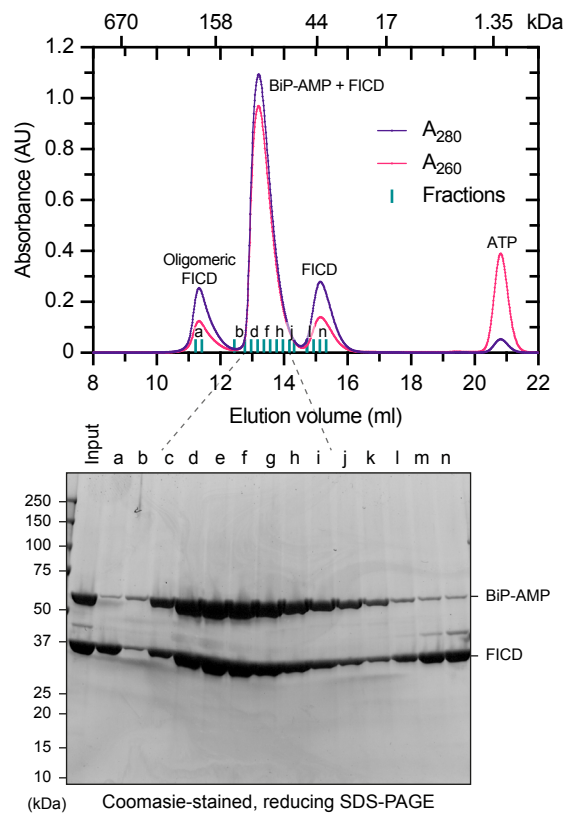
1020

1021 **Fig. 1: The deAMPylation complex crystal structure and mechanism of eukaryotic**
1022 **deAMPylation. a**, FICD's His363Ala mutation facilitates trapping and SEC-based
1023 copurification, of a deAMPylation complex of monomeric FICD and AMPylated BiP.
1024 **b**, The resulting deAMPylation complex crystal structure is colour-coded to illustrate
1025 its (sub)domain organisation. *i*, NBD-based structural superposition with the ATP-state
1026 of isolated BiP-AMP (PDB 5O4P, light grey). *ii*, A focus on the two intermolecular
1027 interaction surfaces. Selected interdomain contacting residues are shown. Polar
1028 interactions are depicted by pink dashed lines. Residues mutated in this study are shown
1029 in green. **c**, Superposition of two heterodimeric crystal structures (purple BiPs and
1030 yellow FICDs) with an FICD dimer structure (PDB 4U0U, grey). In addition the full-
1031 length BiP lid is modelled (green) based on alignment with the BiP:ATP structure (PDB
1032 5E84). Surfaces shown are coloured according to coulombic electrostatic potential.
1033 Note the charge complementarity between the BiP(NBD), visible on the left, and
1034 FICD(TPR1), visible on the right. For illustrative purposes the N-terminal unstructured
1035 region of FICD is shown in the context of an ER membrane. **d**, An unbiased polder-
1036 omit electron density map, contoured at 4σ , covering a region of FICD's active site
1037 (yellow) and BiP's Thr518-AMP (purple). Residues interacting with the AMP moiety
1038 are shown as sticks and the catalytic water is annotated with *. **e**, As in **d** but reduced
1039 to highlight Glu234's coordination of the catalytic water molecule* in-line for
1040 nucleophilic attack into the α -phosphate. Additionally, the general acid His363 is
1041 modelled based on an alignment of PDB 6I7K.

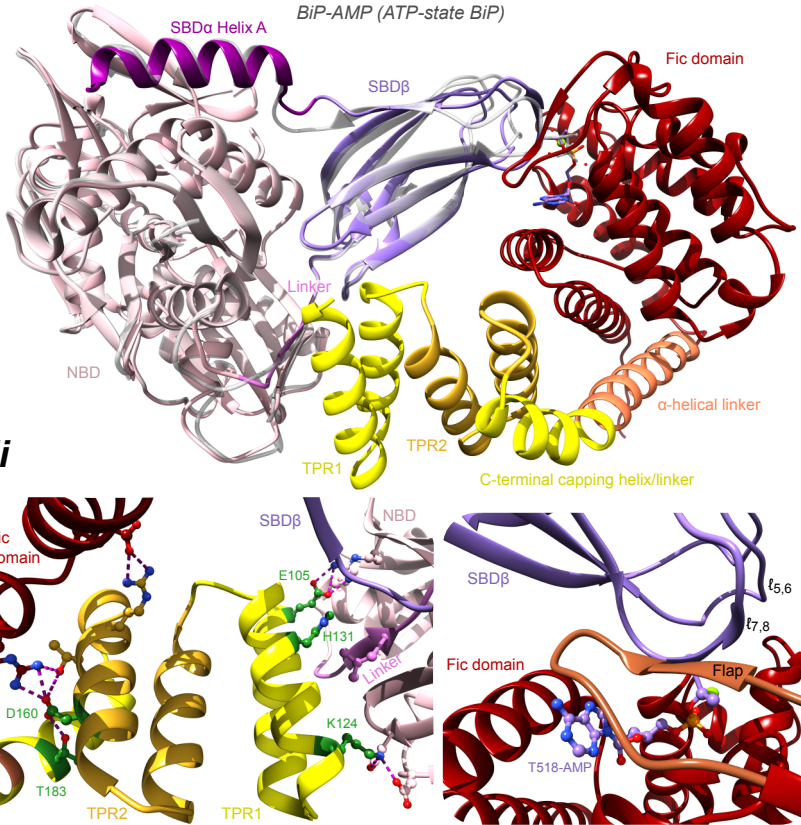
1042

Fig. 1

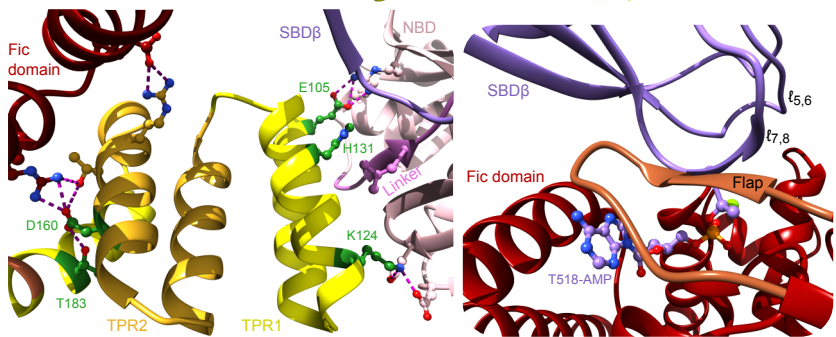
a



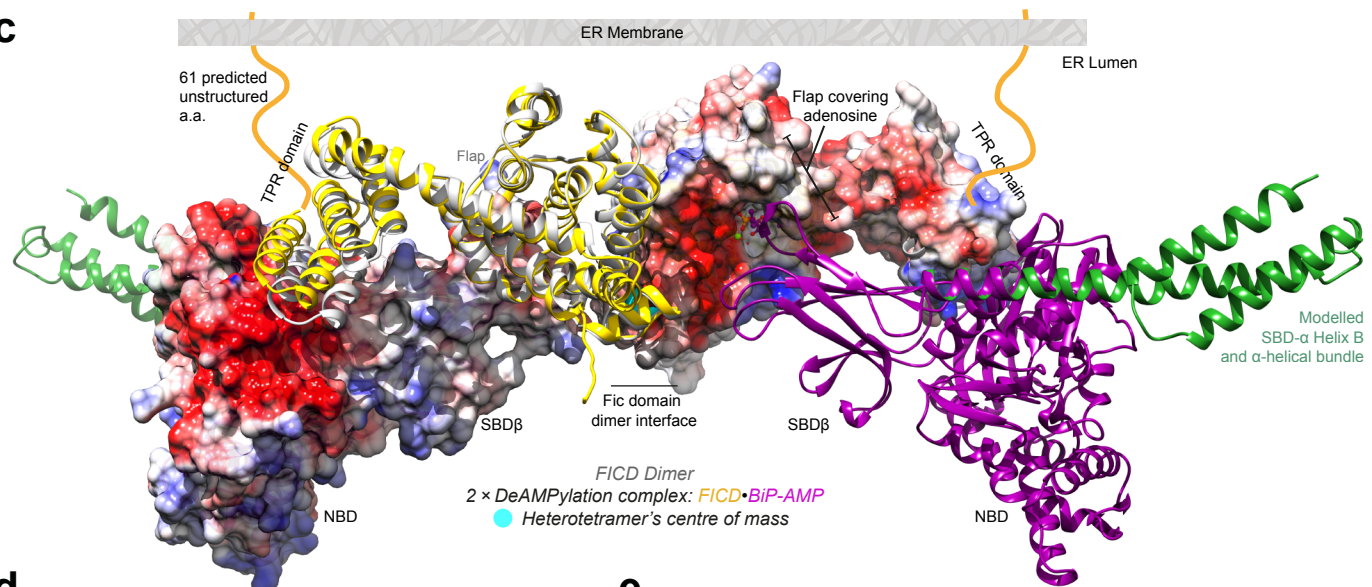
b *i*



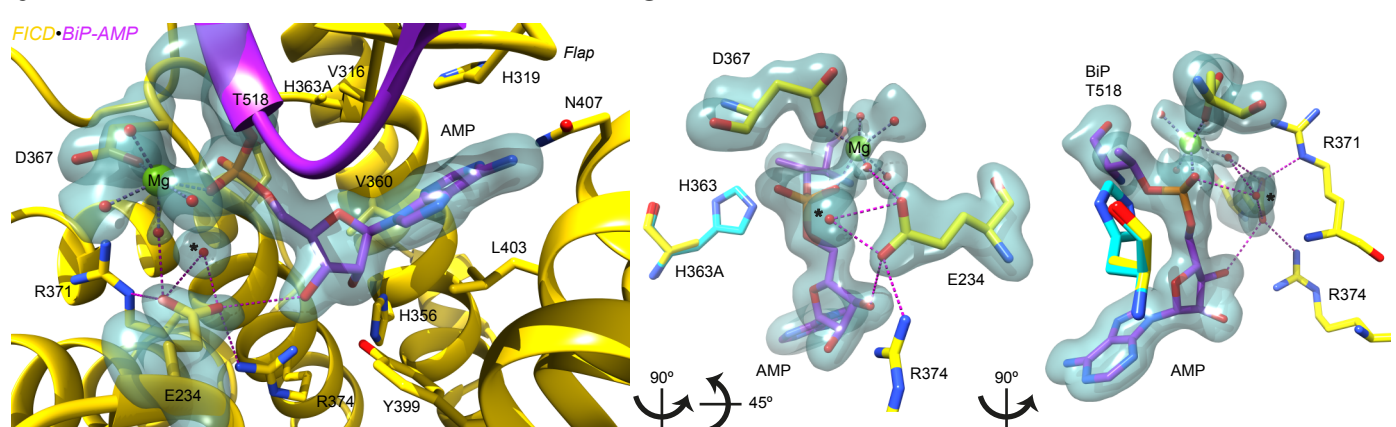
ii



c



e

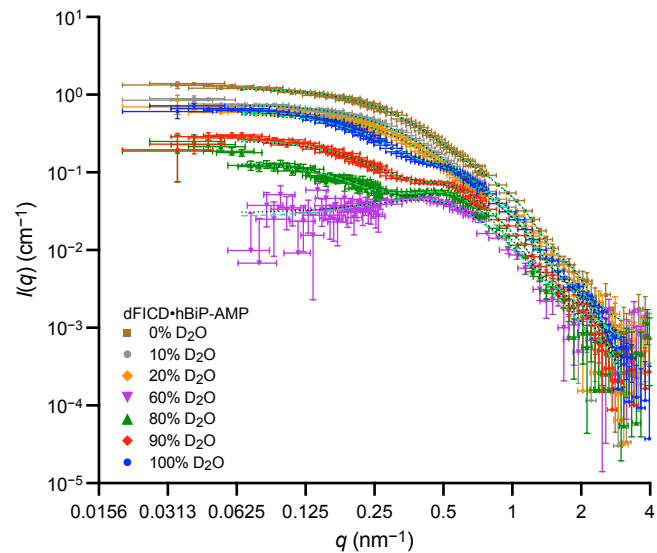
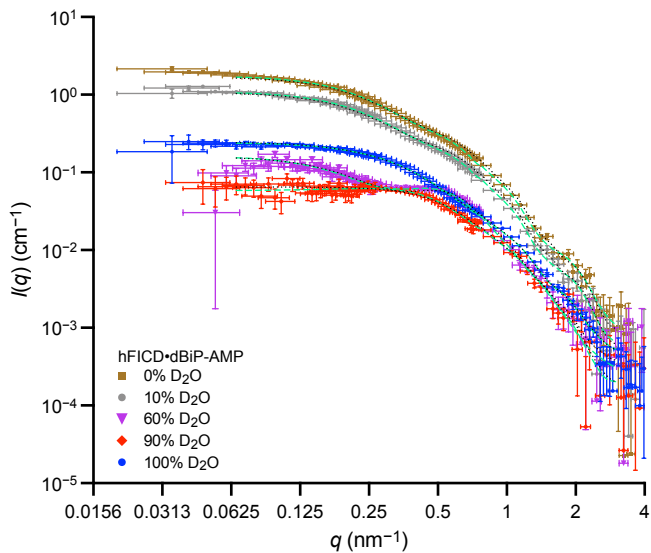


1043 **Fig. 2: The DeAMPylation complex solution structure.** **a**, Contrast-variation small
1044 angle neutron scattering (SANS) curves of copurified dimeric FICD and full-length
1045 AMPylated BiP. Overlaid dotted black lines are theoretical scattering curves based on
1046 the modelled heterotetramer shown in **Fig. 1c**, dashed green lines are the theoretical
1047 scattering curves from flex-fitting of the input heterotetramer model with a constrained
1048 FICD dimer interface. In each experiment ‘d’ and ‘h’ refer to the partially deuterated
1049 and non-deuterated component respectively. Error bars represent SEM with respect to
1050 the number of pixels used in the data averaging. **b**, Guinier plot of partially deuterated
1051 FICD and non-deuterated AMPylated BiP. **c**, Scattering amplitude plots. Linear best-
1052 fits are shown with dashed lines and 95% confidence interval bands are shown with
1053 colour-matched solid lines. **d**, Stuhrmann plot with best-fit dashed curves. 95%
1054 confidence prediction bands are shown with solid lines. The determined match points
1055 of the individual complex components are indicated on the x -axis. Error bars in **c** and
1056 **d** are derived from the standard errors of the Guinier fits. **e**, Optimal flex-fit structures
1057 with respect to overall agreement of theoretical scattering to all experimental contrast-
1058 variation SANS datasets. Output structures are aligned to the input heterotetramer
1059 model, itself derived by imposing the C2 symmetry of the FICD dimer (PDB 4U0U)
1060 onto the heterodimeric deAMPylation complex crystal structure as in **Fig. 1c**.

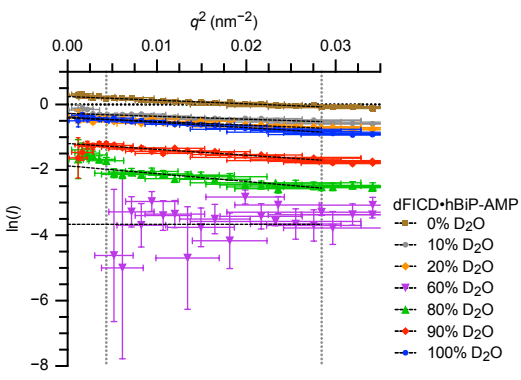
1061

Fig. 2

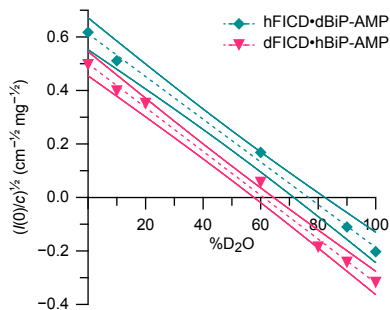
a



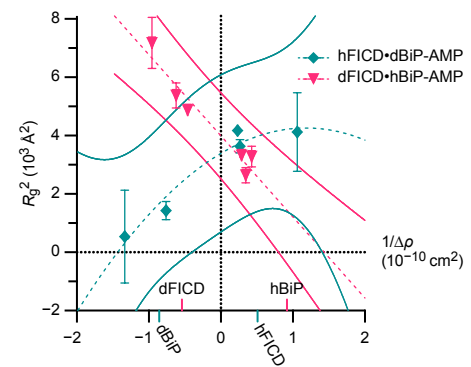
b



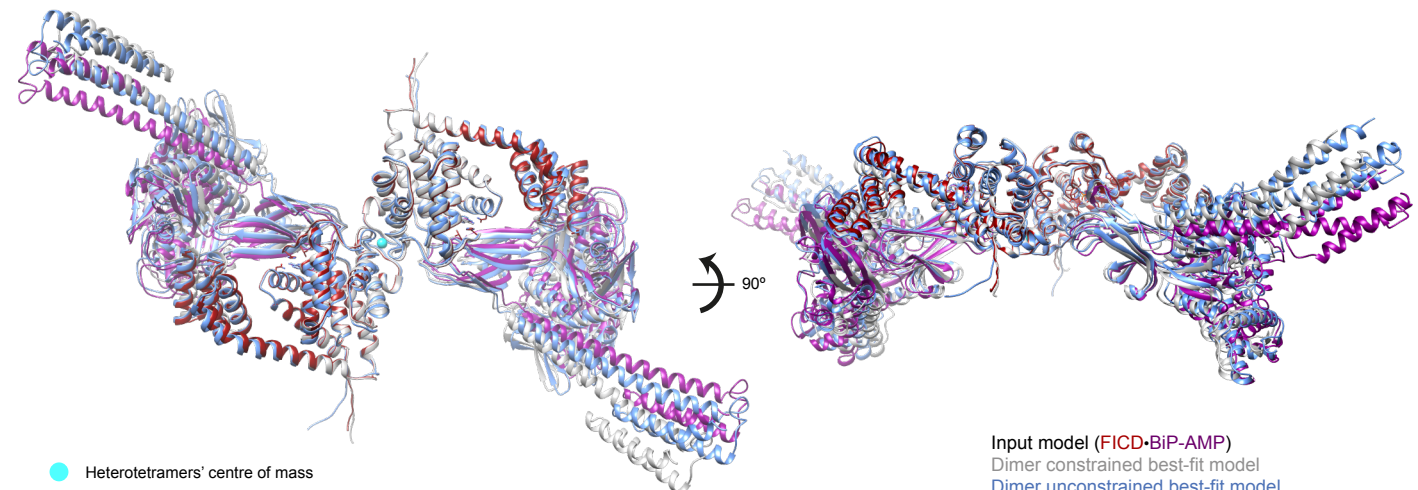
c



d



e

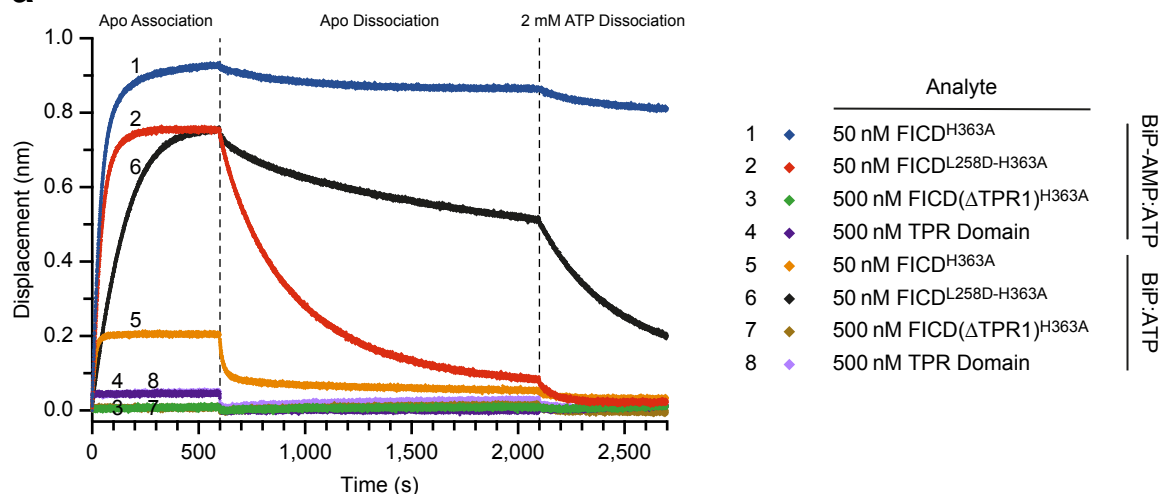


1062 **Fig. 3: FICD's TPR domain is essential for AMPylated BiP binding and**
1063 **deAMPylation.** **a,** Representative BLI association-dissociation curves of FICD
1064 analytes from immobilised BiP bound to ATP (either AMPylated or unmodified), from
1065 $n = 3$ independent experiments. **b,** Representative BLI analysis of TPR domain mutants
1066 of monomeric (*i*) and dimeric (*ii*) FICD binding to immobilised AMPylated BiP, from
1067 $n = 3$ independent experiments. **c,** FP derived analysis of the ability of different FICD
1068 variants to deAMPylate BiP. Left, deAMPylation FP-derived time courses of BiP-
1069 AMP(FAM) deAMPylation. Fits of the initial linear enzyme velocities are overlaid.
1070 Right, resulting quantification of the approximate catalytic efficiencies of the different
1071 FICD variants. Mean values of approximate k_{cat}/K_M values for each FICD variant \pm SD,
1072 from $n = 4$ independent experiments, are shown.

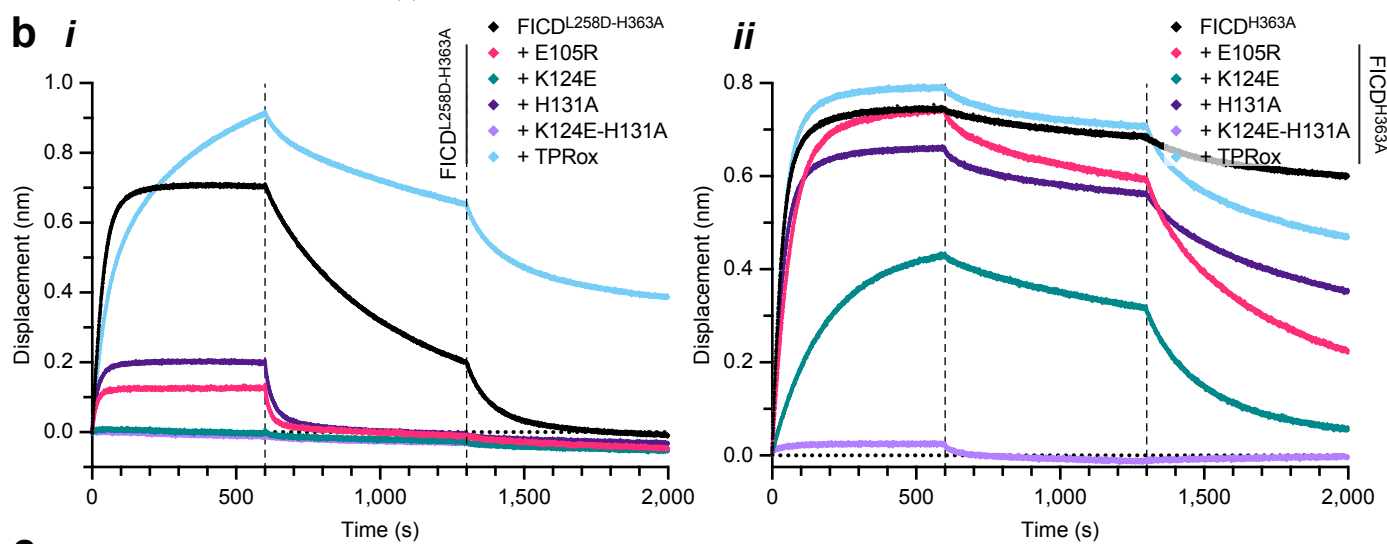
1073

Fig. 3

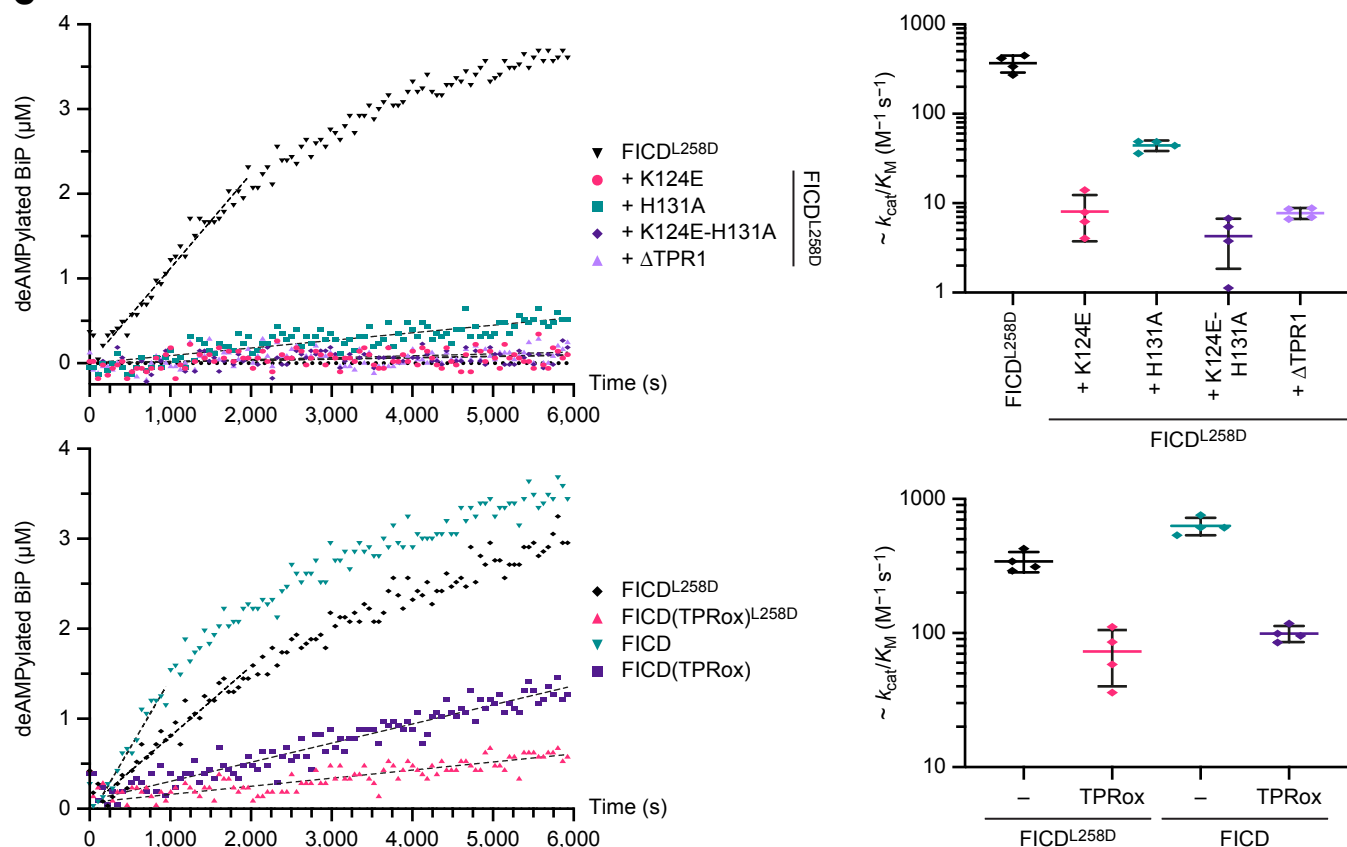
a



b



c

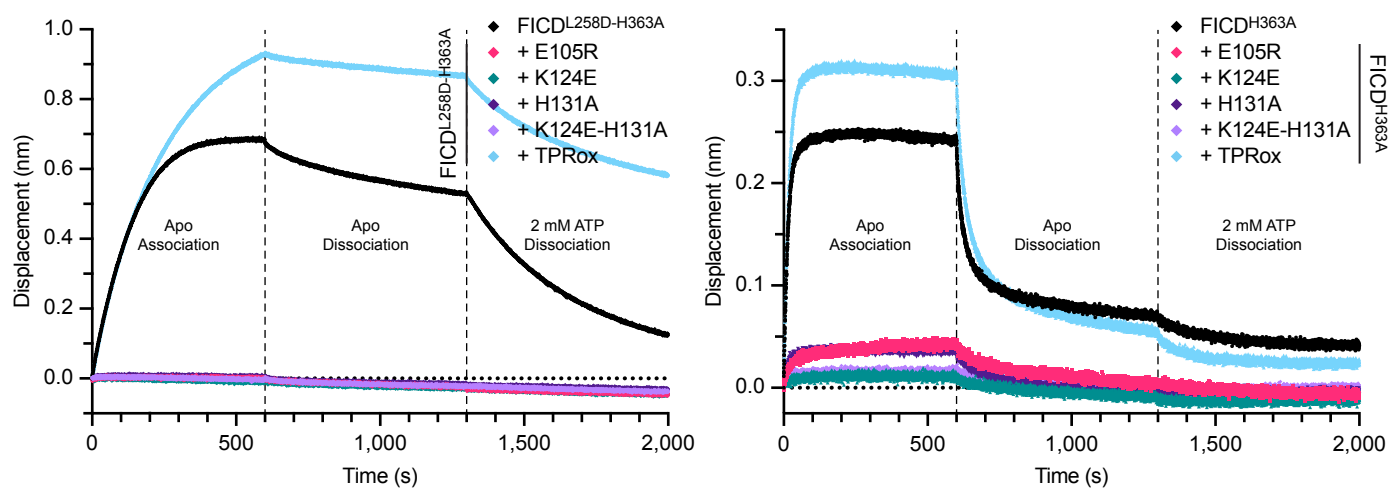


1074 **Fig. 4: FICD's TPR domain is essential for the recognition and AMPylation of**
1075 **ATP-bound BiP. a,** Representative BLI analysis of TPR domain mutants of
1076 monomeric (*i*) and dimeric (*ii*) FICD binding to immobilised ATP-bound BiP, from n
1077 = 3 independent experiments. **b,** Fluorescence and Coomassie gel-images of an in vitro
1078 AMPylation assay, utilising ATP(FAM) as the AMPylation co-substrate, in the
1079 presence of excess product trap (Trap(ox)) to discourage BiP-AMP(FAM)
1080 deAMPylation. dFICD, dimeric FICD; mFICD, monomeric FICD^{L258D}. Gels from a
1081 representative experiment are shown with the initial rates (mean ± 95% CI) of BiP-
1082 AMPylation (in relative fluorescent units/s), normalised to the rate of mFICD-mediated
1083 BiP-AMPylation, from n = 4 independent experiments. Note, the lack of correlation
1084 between FICD (*cis*)auto-AMPylation and BiP substrate AMPylation. **c,** Native-PAGE
1085 immunoblot analysis of the accumulation of AMPylated (B-form) BiP in *FICD*^{-/-} CHO
1086 cells transfected with FICD variants, as indicated. Major, non-AMPylated BiP species
1087 (A, II and III) are noted. Right, quantification of AMPylated B-form BiP from n = 3
1088 independent experiments (mean ± SD). **d,** Histograms of the FACS signal of an
1089 XBP1::Turquoise UPR reporter in *FICD*^{-/-} CHO cells expressing the indicated FICD
1090 derivatives. Note the bimodal distribution of the fluorescent signal in FICD-transfected
1091 cells. Quantification of the fraction of cells that are stressed, as well as the median
1092 FACS signal of the low and high stressed cell populations are shown from n = 4
1093 independent experiments (mean values ± SD). Bars and datapoints are (colour-)coded
1094 according to the histogram legend.

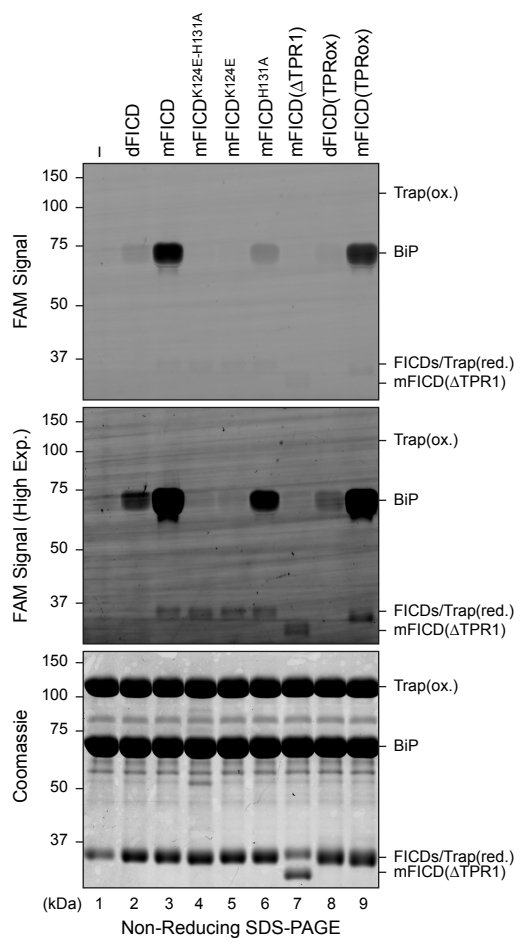
1095

Fig. 4

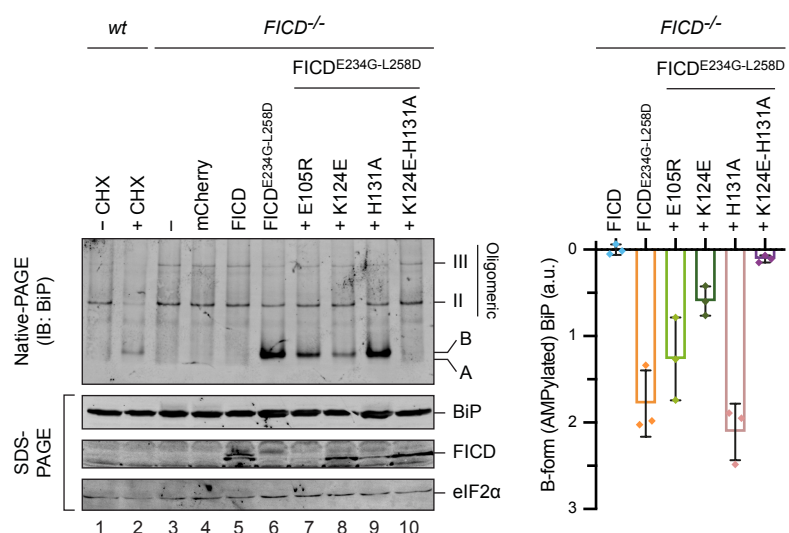
a



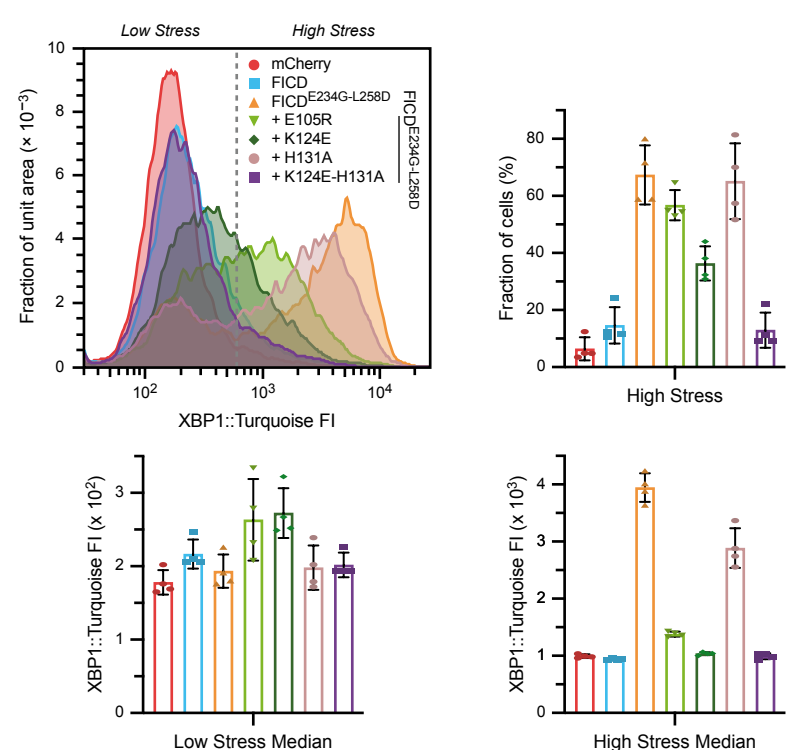
b



c



d

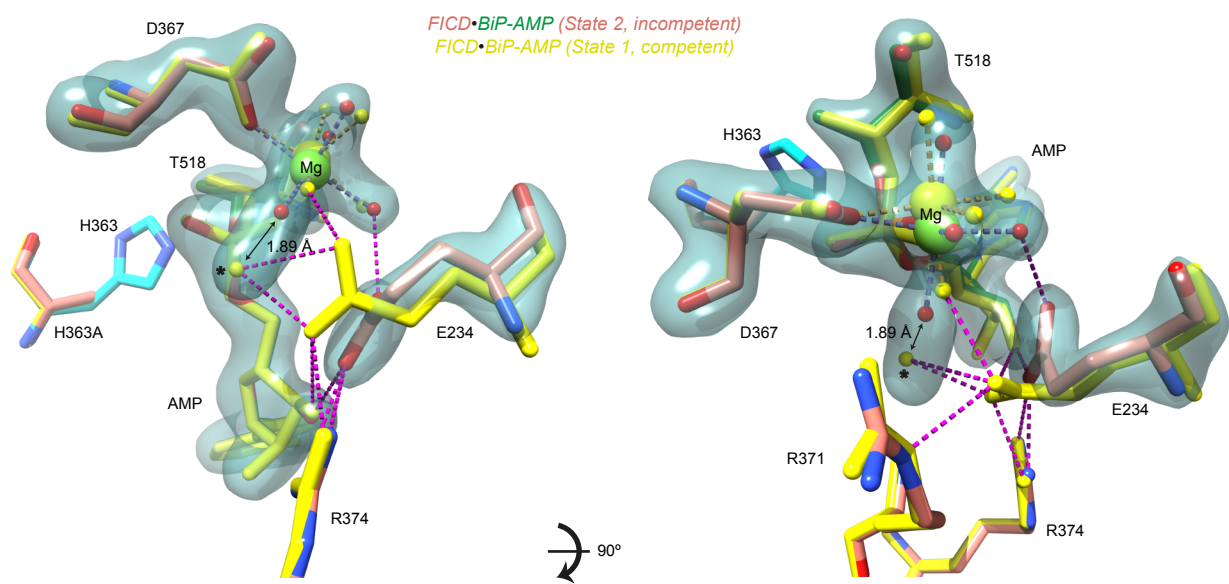


1096 **Fig. 5: FICD monomerisation increases gatekeeper Glu234 flexibility and**
1097 **decreases the deAMPylation k_{cat} .** **a**, An unbiased polder-omit electron density map
1098 from a second deAMPylation complex structure (state 2), contoured at 6σ , covering Fic
1099 domain catalytic residues of particular importance (orange), the Mg^{2+} -coordination
1100 complex and BiP's Thr518-AMP (green). The reduced (state 2) active site is aligned
1101 with the active site of the (deAMPylation competent) state 1 complex (yellow). His363
1102 is modelled from an alignment of catalytically competent FICD (PDB 6I7K, as in **Fig.**
1103 **1e**). Residues interacting with the AMP moiety are shown as sticks and the catalytic
1104 water (from state 1) is annotated with *. The distance between the Mg^{2+} first-
1105 coordination sphere water (red, state 2) and the (state 1) catalytic water* is annotated.
1106 H-bonds formed by Glu234 are shown as pink-dashed lines. **b**, A representative BiP-
1107 deAMPylation time course with $10 \mu\text{M}$ FICD or $\text{FICD}^{\text{L258D}}$, demonstrating that 100
1108 and $150 \mu\text{M}$ BiP-AMP both represent saturating concentrations of deAMPylation
1109 substrate. **c**, The derived k_{cat} parameters, from $n = 4$ independent experiments with two
1110 saturating concentrations of BiP-AMP (as in **b**). The mean \pm SD is shown with the P -
1111 value from a two-tailed Welch's t -test annotated.

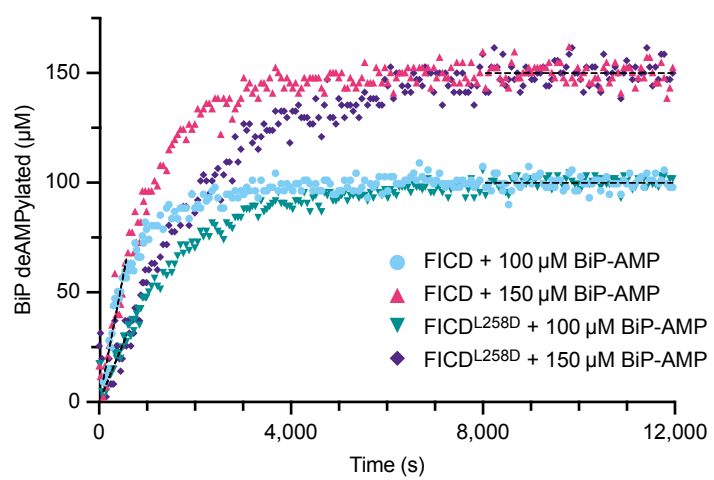
1112

Fig. 5

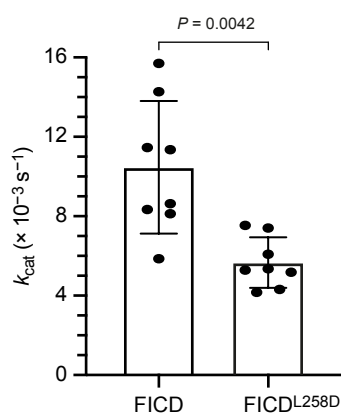
a



b



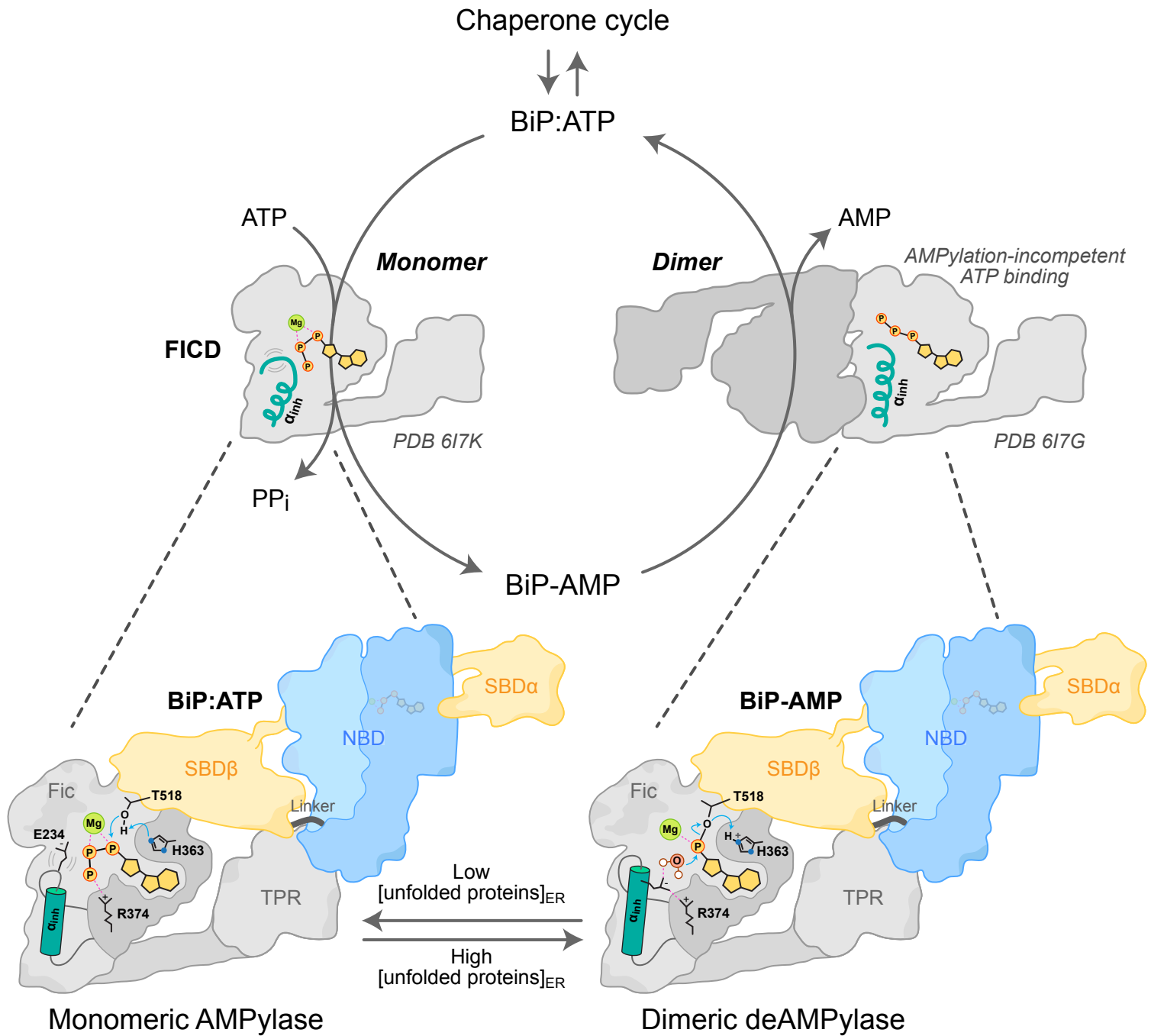
c



1113 **Fig. 6: Model of FICD AMPylation and deAMPylation of BiP.** FICD recognises
1114 (AMPylated or unmodified) BiP's linker-docked NBD and the $\ell_{7,8}$ region of the SBD β ,
1115 via its TPR and catalytic domain, respectively. This is only possible when BiP is in a
1116 domain-docked ATP-like state. Dimeric FICD has a relatively rigid gatekeeper Glu234
1117 which facilitates efficient alignment of an attacking water for BiP deAMPylation whilst
1118 prohibiting AMPylation competent binding of ATP. Conversely, monomeric FICD has
1119 a more flexible Glu234 which decreases its deAMPylation efficiency whilst permitting
1120 AMPylation competent binding of MgATP. The FICD monomer-dimer equilibrium is
1121 adjusted in response to changing levels of unfolded proteins within the ER by a yet-to-
1122 be discovered process.

1123

Fig. 6



1124

1125

1126

1127

1128

1129

1130

1131

1132

1133

1134

1135

1136

1137

1138

1139

1140

1141

1142

1143

1144

1145

1146

1147

1148

1149

1150

1151

	FICD•BiP-AMP DeAMPylation (State 1)	FICD•BiP-AMP DeAMPylation (State 2)
<i>Data collection</i>		
Synchrotron stations	DLS I04-1	DLS I04-1
Space group	<i>P</i> 2 ₁ 2 ₁ 2	<i>P</i> 2 ₁ 2 ₁ 2
Molecules in a.u.^a	2 (2)	2 (2)
a,b,c; Å	95.37, 104.08, 105.63	95.00, 103.89, 104.79
α, β, γ; °	90.00, 90.00, 90.00	90.00, 90.00, 90.00
Resolution, Å	105.63-1.70 (1.73-1.70)	52.40-1.87 (1.92-1.87)
R_{merge}	0.085 (1.299)	0.087 (1.793)
<I/σ(I)>	10.3 (1.2)	11.9 (1.0)
CC1/2	0.992 (0.585)	0.999 (0.536)
No. of unique reflections	115633 (5639)	86247 (6270)
Completeness, %	99.8 (99.3)	100.0 (100.0)
Redundancy	6.6 (6.5)	6.6 (6.9)
<i>Refinement</i>		
R_{work}/R_{free}	0.195 / 0.221	0.177 / 0.231
No. of atoms (non-H)	7868	7575
Average B-factor, Å²	29.0	37.4
RMS Bond length, Å	0.003	0.003
RMS Bond angle, °	1.171	1.199
Ramachandran favoured region, %	98.37	98.49
Ramachandran outliers, %	0	0
MolProbity score^b	0.81 (100 th)	1.04 (100 th)
PDB code	7B7Z	7B80

Table 1: Data Collection and refinement statistics. Values in parentheses correspond to the highest-resolution shell, with the following exception: ^aThe number of molecules in the biological unit is shown in parentheses (a.u., asymmetric unit cell). ^bThe MolProbity score as a percentile is shown in parentheses, higher is better.